Remote Material Characterization using mmWave FMCW Radar with Complex Baseband

by

Ahmed Metwally Hegazy

A thesis
presented to the University of Waterloo
in fulfillment of the
thesis requirement for the degree of
Master of Applied Science
in
Electrical and Computer Engineering

Waterloo, Ontario, Canada, 2020

Author's Declaration

I hereby declare that I am the sole author of this thesis. This is a true copy of the thesis, including any required final revisions, as accepted by my examiners.

I understand that my thesis may be made electronically available to the public.

Abstract

Material characterization has been a topic of interest for many years due to numerous applications in industry and research. Free space material characterization has seen lots of interest lately due to the non-invasive and non-destructive nature of the measurement procedure which is an important feature for some applications such as medical, food quality and production lines applications. In this thesis, a new method for characterizing materials and extracting parameters like dielectric constant, loss tangent and thickness, is presented. The method relies on using Frequency Modulated Continuous Wave (FMCW) radars with complex baseband to extract those features from both the magnitude and phase of the reflection coefficient of the material. Our study shows that utilizing both the magnitude and phase can enhance the accuracy of measurement and provide some extra information regarding the material configuration e.g., dielectric suspended in air or placed on a metal substrate. Using FMCW radar in free-space material characterization is a very good alternative to traditional free-space methods which rely on expensive and bulky VNAs. Two dielectric materials were tested, and the results were compared to data from literature.

Acknowledgements

I would like to thank everyone who helped me reach this milestone. First, I would like to express my sincere gratitude to Professor Safavi-Naeini for giving me the opportunity to be part of a great research community like the Centre for Intelligent Antenna and Radio Systems (CIARS), and for being a great supervisor and professor. I want to thank Dr. Mohamed Basha for giving me the opportunity to learn and contribute by joining the research activities led by him, and for his valuable guidance and mentorship. I would like to thank my colleague Mostafa Alizadeh for helping me with the radar testing and for his valuable advice throughout the project. Also, I would like to thank my friends Amr Samir and Mahmoud Mabrouk for their continuous and valuable support and for being great friends. Special thanks to Chris Schroeder, for taking the time to help me improve my writing and for her administrative support and dedication. I wish also to extend special gratitude to Al Ghurair Foundation for Education (AGFE) for their generous financial and educational support provided throughout my studies. Last but not least, thanks to my beloved family in Egypt for their unconditional love and support.

Dedication

This thesis is dedicated to my beloved parents, sister and brother for their support, for being a part of my life, and for believing in me.

Table of Contents

List of Tables

List of Figures

Chapter 1

Introduction

1.1 Motivation

Accurate extraction of material parameters like dielectric constant and dielectric loss is very important for many applications that either use these materials as part of a larger design like RF/Microwave applications [10] and PCB manufacturing [47], or in applications like food quality [1] and non-invasive medical testing [3]. There are numerous ways for extracting those parameters including cavity-resonance based methods [48] and one-Port or two-Port waveguide based methods in [44], [19] and [2] . Some of these methods require direct contact with the sample material and others are non-contact or non-invasive which are also known as free-space methods as discussed in [32],[13] and [30]. Most of these methods rely on a bulky and expensive VNA to extract reflection or transmission parameters for these materials and also require special sample preparation. Radar transceivers are a promising alternative to VNA for extracting reflection coefficient for characterizing materials [43]. These radar transceivers are very compact and low-cost and can characterize the material from a distance which makes them ideal for application requiring non-invasive testing. Some of these applications are medical testing for tumor detection, testing material and products in production line, testing food quality and quick characterization for materials used in RF applications e.g. dielectric resonator.

Due to the fact that most modern automotive applications use FMCW radars for collision avoidance and safety [35], means that adding the material characterization feature to these radars can also provide an additional data about the target needed for taking the proper action e.g. identifying human targets through fog or rain. The work in this thesis represents an early study for the use of a complex baseband radar system with a special

waveform (FMCW) in the 77 GHz band which is very common for automotive applications, for extracting dielectric properties and configuration information about the target material. The use of both magnitude and phase information of the complex baseband of the radar is found to be a good way for enhancing the measurement accuracy and providing more information about the target.

1.2 Research Objectives

The main objectives of this research are:

- Exploring the possibility of using FMCW radar with complex baseband for free space material characterization.
- Studying the possibility of utilizing the phase information in the reflection factor to enhance the measurement accuracy and identifying material configuration.
- Deriving the theoretical foundations for complex FMCW material characterization.
- Exploring possible applications and studying the limitations for using FMCW for free space material characterization.

1.3 Thesis Layout

This thesis is organized in 6 chapters starting with the introduction. In Chapter 2, a general literature review about free-space material characterization is discussed. The review starts with a discussion for general free-space material characterization methods including transmission and reflection based methods. Additionally, several reflection based methods are further reviewed with a discussion for their applications and limitations. An early study for the usage of ultra wide band real-only FMCW radar is discussed with its advantages and drawbacks.

In Chapter 3, we introduce the full theoretical foundations and the different models for our problem. Three models are discussed, transmission line and reflection model for the problem of a dielectric slab backed by air or metal, and a complex baseband FMCW model for the same problem. Furthermore, an extension for the previous models for the problem of multi-layer dielectric is introduced. The difference between different types of dielectrics and their corresponding reflection factor magnitude and phase is examined with

emphasis on the phase information importance in enhancing the measurement accuracy and identifying the material layer configuration. Additionally, some MATLAB simulations for the aforementioned models are introduced.

In Chapter 4, the FMCW Radar board used for our research is reviewed in detail. The used board is AWR2243 77GHz FMCW radar from Texas Instruments with 3 Tx and 4 Rx channels. In order to obtain maximum reflection from the target material, a lens has to be used with the radar. A 3D-Printed hyperbolic lens was designed and fabricated for the Tx and Rx antennas used in the TI radar board. The lens design and fabrication is discussed in detail in Chapter 5 with a brief discussion of types of lenses that can be used for the same purpose with their advantages and drawbacks.

Chapter 6 introduces the experiment results that were accomplished on different materials to verify our theoretical models and simulations. Finally, Chapter 7 discusses the future work needed for enhancing the system capabilities and enabling an automatic calibration process by adding extra sensors to the system.

Chapter 2

Background and Literature Review

Measuring the dielectric properties of materials and samples is a very important process for many research and industrial domains such as absorber material and circuit board substrates characterization for microwave applications, food ripeness research, biological and tissue engineering etc. [46], [45], [28]. The aim of these methods is to measure and estimate the dielectric parameters of the material under test including the dielectric constant ϵ_r and loss tangent tan δ.

The dielectric parameters of a material are fundamentally the complex permittivity ϵ and complex permeability μ. The real part of the complex permittivity, represents the amount of energy stored in the material due to an external electric field. On the other hands, the imaginary part represents the amount of energy lost or dissipated inside the material as a result of an external electric field. This value is equal to zero for lossless materials. The ratio between the imaginary part and the real part of the complex permittivity is known as the loss tangent tan δ. For the complex permeability, the real part represents stored energy in the material resulting from an externally applied magnetic field, and the imaginary part represents the lost energy in the material due to the same magnetic field. For dielectric material, the value of the complex permeability is very close to free space permeability [5], [45]. Table 2.1 below shows some material examples with their values for dielectric constant and loss tangent measured at 2.45 GHz.

Most of the material characterization methods rely on the transmission and reflection coefficients for extracting the dielectric parameters. There are many methods that have been developed for measuring the transmission and reflection coefficient data from the material and algorithms derived for estimating the dielectric parameters from the processing of these measured data [31],[15],[29]. In this chapter, we are going to review these mea-

Material	ε_r	tanδ
Teflon	2.1	0.0003
Alumina	9	0.0006
Glass Ceramic	6	0.005
Concrete (Dry)	4.5	0.0111
Wood	1.2-5	0.004-0.4167

Table 2.1: Examples of materials and their dielectric properties at room temperature and 2.45 GHz frequency [45]

surement methods and briefly go through the algorithms used with them. Additionally, more detailed discussion on some interesting examples of those techniques are presented [45]. The measurement methods can be mainly classified into four categories based on the technique used. Those methods are:

- Resonance Method
- One-Port Method
- Two-Port Method
- Free-Space Method

2.1 Resonance Method

In the Resonance method, a material sample is shaped and placed in a cavity resonator and the change of the resonance frequency and the quality factor is monitored. Before that, the resonance frequency and the quality factor Q of this cavity, which is defined as the frequency/bandwidth ratio, are measured when it is empty [46]. The resonance frequency and the quality factor shift from the empty cavity to cavity filled with material sample, as shown in Figure 2.1, has a direct relationship with the dielectric constant ε_r and loss tangent tan δ of the sample material according to equations 2.1 and 2.2 which were introduced in [34].

$$\varepsilon_s' = \frac{A\varepsilon_r' V_c}{V_s}\left(\frac{f_c - f_s}{f_s}\right) + \varepsilon_r' \tag{2.1}$$

$$\varepsilon_s'' = \frac{BV_c}{V_s}\left(\frac{\varepsilon_r'^2 + \varepsilon_r''^2}{\varepsilon_r'}\right)\left(\frac{Q_c - Q_s}{Q_c Q_s}\right) + \frac{\varepsilon_s'\varepsilon_r''}{\varepsilon_r'} \tag{2.2}$$

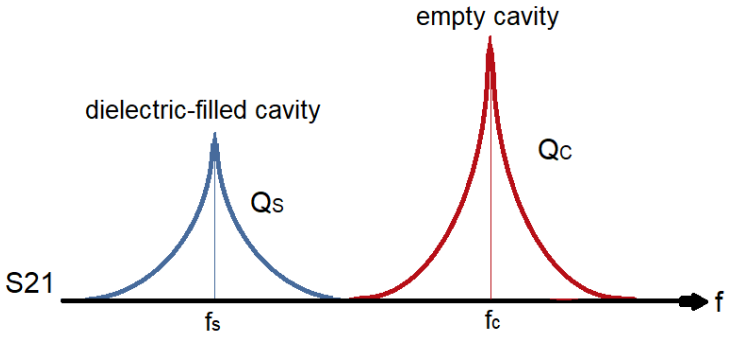

Figure 2.1: Change of the resonance frequency and the quality factor Q after inserting the material.

where ε' and ε'' represent the real and imaginary parts of the complex permittivity respectively; the subscripts r and s represent the material of the cavity, and the sample being measured respectively (for air filled cavity ε_r'=1 and ε_r''=0). Moreover, f_C and f_S are the resonance frequencies of the empty and sample filled cavity respectively, Q_C and Q_S are the quality factors of the empty and sample filled cavity , V_c is the cavity volume and V_s is the volume of the sample. Finally, A and B are constants that depend on the geometry of the cavity [34].

This method is very accurate especially with low loss materials. However, in order to achieve this high accuracy, a VNA with very high frequency resolution is needed for detecting the finest frequency shift (e.g., 1 Hz) [45].

There are some reported techniques which use a cavity made into a substrate integrated waveguide SIW which is compact and easy to manufacture compared to conventional cavity resonators. It can also be used to characterize liquid samples as discussed in [26].

Despite the accuracy of this technique, it suffers from some drawbacks such as the limited frequency band for measurement due to the nature of the cavity resonance principle. The sample also needs to be prepared and shaped before the measurement. Furthermore, it needs a very high resolution and complex VNA for an accurate measurement.

2.2 One-Port Method

The second method is the one-port method which relies on reflection coefficient measurement of a material sample terminating an open-ended waveguide. This waveguide can be either a coaxial or a rectangular waveguide [46]. The basic principle behind this method is that the reflected signal in an open-ended waveguide terminated by the material sample, will be affected by the presence of that sample so that the reflection coefficient S_{11} will contain information about the material dielectric properties. This S_{11} is measured using a VNA and post-processed to extract the desired parameters [45].

Due to the presence of the waveguide between the VNA cable and the material sample, a standard one port calibration process must be done before doing the measurements. This step is known as de-embedding. The error terms added by the presence of the waveguide are removed by using the conventional TRL (Thru-Reflect-Line) calibration method used in VNA. After de-embedding, the measurement reference plane is transplanted to the surface of the sample material.

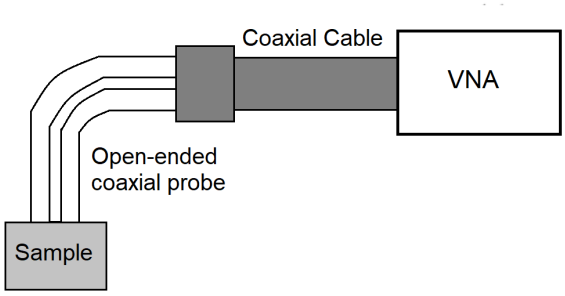

Figure 2.2: Coaxial probe based one-port measurement setup with material sample.

Figure 2.2 above shows the different components of the measurement system using the open-ended waveguide method with a coaxial probe for characterizing a tissue sample. The calibration or de-embedding is done first to translate the connector plane to the probe end or the material surface shown in the figure as aperture plane. The reflection coefficient measurement is then used to calculate the dielectric parameters of the material [45].

Figure 2.3 shows different configurations for the open-ended waveguide method using coaxial waveguide for thick a) and thin b) samples and similar for rectangular waveguide probe c) and d). Both the rectangular waveguide and coaxial probes are suitable for thin film samples when supported by metal as shown in 2.3(b),(d). For thicker samples, the rectangular waveguide is generally used with larger sample dimensions due to the much larger radiation distance (20 cm for WR90).

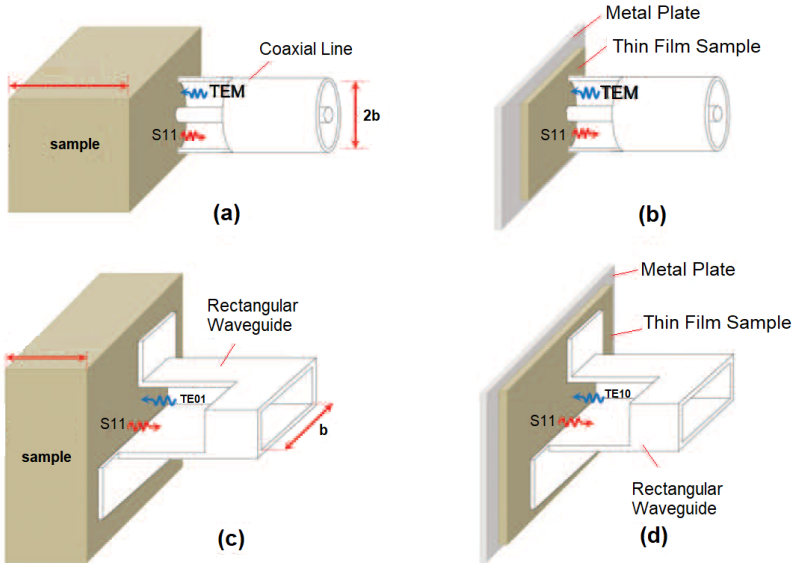

Figure 2.3: Different configurations for one-port measurement setup with coaxial transmission line a), b) and rectangular waveguide c), d) [46] (Reused under a CC-BY license)

This method is non-destructive and requires no special shaping or preparation for the sample material. However, it is required that the probe is in close contact with the sample . Additionally, air gaps between the probe and the sample introduces extra errors.

2.3 Two-Port Method

The third method is the Two–Port method utilizing both reflection and transmission characteristics of the material under test. This method is very similar to the One-Port method previously discussed in the general principle of calculating the dielectric properties of the material from the measured S parameters using a waveguide probe and VNA. However, in this method, the material sample is placed inside a waveguide and both reflection and transmission coefficients, S_{11} and S_{21} respectively are measured as seen in Figure 2.4. The dielectric constant is then calculated from both those parameters [46].

Due to the use of the waveguide, which can be a rectangular or coaxial, a good calibration is required before doing the measurement. This calibration can be done by two methods: The first one is by compensating the phase error added by the waveguide length before and after the sample material to translate the measurement plane from the connector

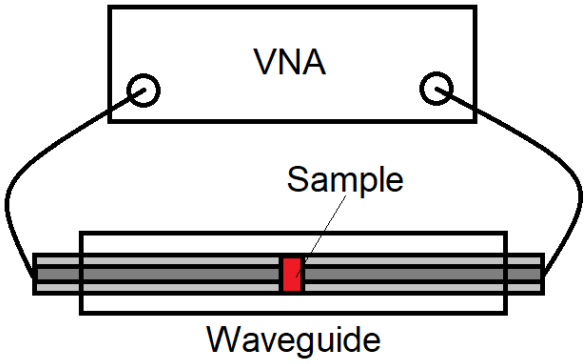

Figure 2.4: Two-port measurement setup with rectangular waveguide [45]

to the sample material surface. The second method is using the standard TRL calibration technique for VNA similar to the open-ended waveguide method. This technique is good for measuring samples with high loss [45], and also capable of measuring both permittivity and the permeability of sample material unlike the open-ended method which is only able to measure permittivity [45]. However, this method needs special preparation and shaping for the sample material to fit inside the waveguide as shown in Figure 2.5, which makes it a destructive method.

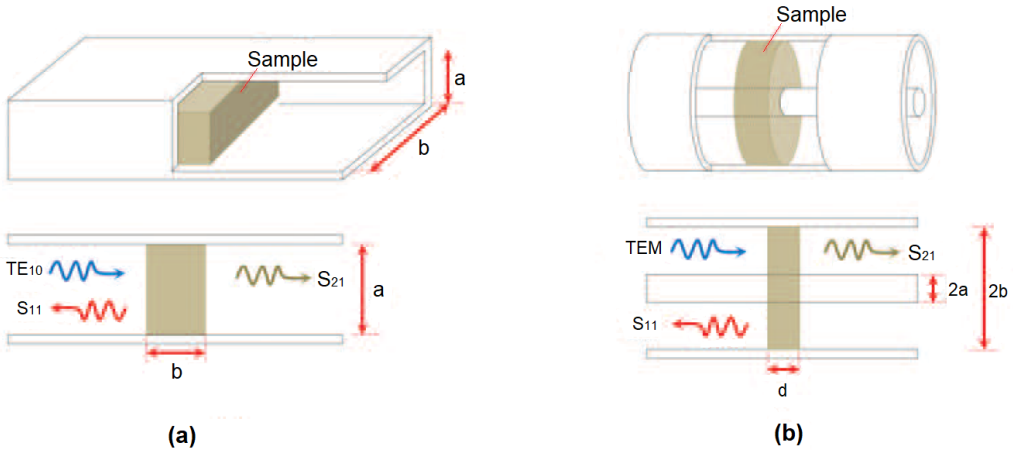

Figure 2.5: Different configurations for two-port measurement setup with coaxial transmission line a) and rectangular (Reused under a CC-BY license).

2.4 Free-Space Method

The fourth and the last material characterization technique, and the one of which our proposed work is based on is the Free-Space method. In this method, the material and the probes or the measurement setup are separated and not in contact with each other. This kind of measurement is mainly used for applications where the access to the material under test is restricted or could damage the measurement equipment. For example, characterizing a material placed in a furnace or a production line. The setup for this method consists of a transmit and receive antennas (usually horn antennas) connected to a VNA for measuring the S-Parameters of the material which is separated from the antennas by a certain distance.

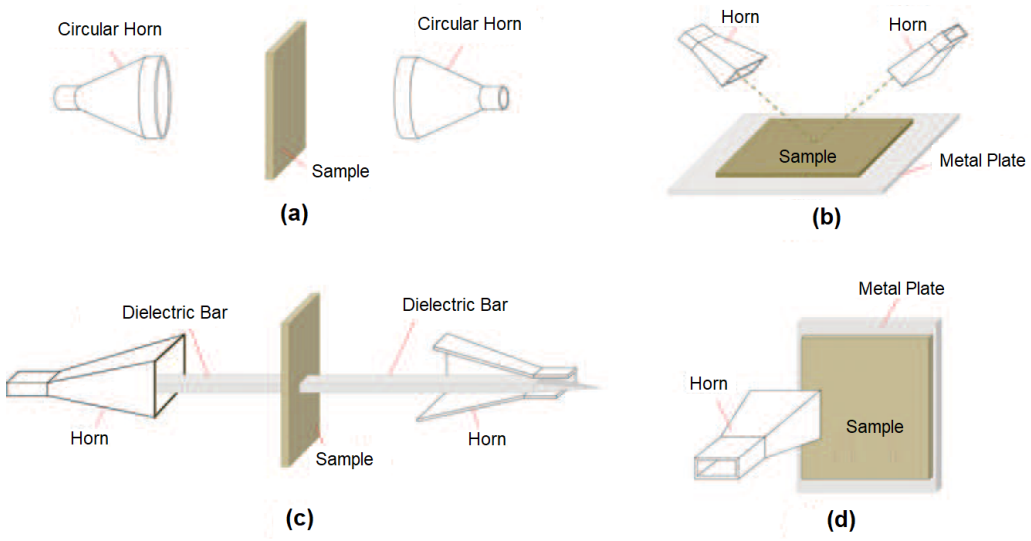

Figure 2.6: Various configurations for free-space measurement setup [46] (Reused under a CC-BY license)

There are various configurations used depending on the transmit and receive antennas setup and which S parameters are used for the characterization as shown in Figure 2.6. Some configurations rely on the transmission parameters only as seen in Figure 2.6(a),(c). Other rely on the reflection parameters as shown in Figure 2.6(b),(d).

One of the common configurations for this method is using the two antennas facing each other with the material between them as shown in Figure 2.7. This method utilizes the transmission coefficient S_{21} for calculating the dielectric properties of the material. Other configurations have the antennas located beside each other and directed towards

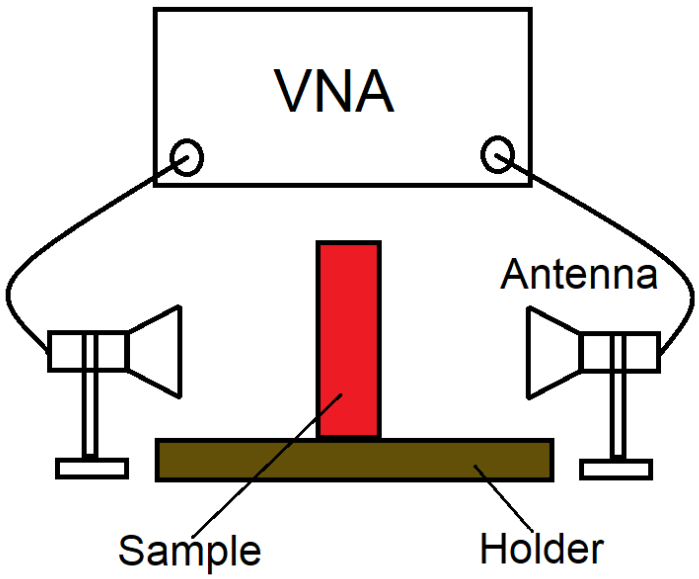

Figure 2.7: Free-space measurement setup.

the material utilizing the reflected signal from the material. In all cases, the measurement setup needs to be calibrated before starting the measurement. The calibration is done in order to remove the effect of the antennas and the separation between the antennas and the material. After the calibration, the measurement reference plane is translated to the material surface.

Free-space method is non-contact and non-destructive. However, it requires flat and relatively large samples for measurements. One of the problems with the free-space method is the multi-reflections between the antennas and the material, and multi-path reflections from the environment around the setup which requires that the test is done inside an anechoic chamber for accurate measurements.

In [37] , researchers tried to mitigate this problem by proposing a technique for reducing the multi-path reflections from the environment by doing several tests while rotating the setup in multiple directions and changing the separation distance between the material and the antennas and then averaging the results to cancel out the multi-patch reflections from the walls. The setup they use consists of a VNA connected to two antennas close to each other and directed at the material which is located at some distance away. The angle of incidence could be assumed to be equal to 0 as the two antennas are very close to each other as shown in Figure 2.8.

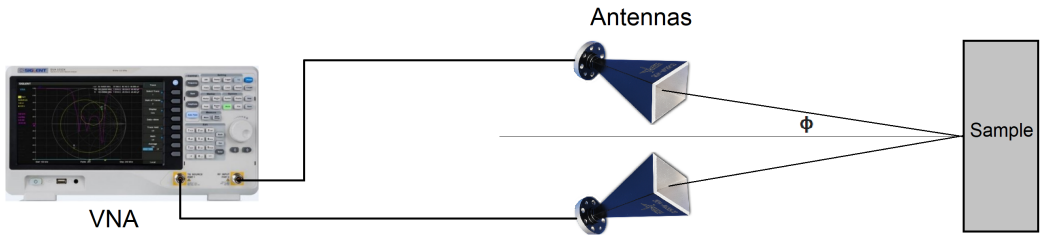

Figure 2.8: Free-space measurement system used in [27]

The de-embedding is preformed by first considering that the parameter S_{21}, measured by the VNA, is equal equation 2.3.

$$S_{21}^{\text{total}} = B\frac{e^{-2jk_0R}}{2R}\Gamma^{\text{MUT}} + A \tag{2.3}$$

where A and B are the antenna mutual coupling and the incident wave amplitude respectively. The distance between the material and the antennas is expressed by R while k_0 is wave number. Γ^{MUT} represents the reflection coefficient at the surface of the material which contains the information about its dielectric properties. This simply means that the S_{21} seen by the VNA is nothing but the reflection coefficient at the surface of the material attenuated and phase shifted with the antenna mutual coupling added to it. In order to extract this reflection coefficient, A and B has to be determined. In order to extract the mutual coupling A, a test without the material is preformed to measure only the coupling of the two antennas:

$$S_{21}^{\text{antennas}} = A \tag{2.4}$$

Another test is completed with the material replaced by the its metallic equivalent:

$$S_{21}^{\text{metal}} = -B\frac{e^{-2jk_0R}}{2R} + A \tag{2.5}$$

From those 3 tests, Γ^{MUT} can be extracted easily using the following formula:

$$\Gamma^{\text{MUT}} = \frac{S_{21}^{\text{total}} - S_{21}^{\text{metal}}}{S_{21}^{\text{antennas}} - S_{21}^{\text{metal}}} - 1 \tag{2.6}$$

As mentioned previously, this embedding and testing is done N times with different distances and changing the setup direction inside the room. All the results are then summed and divided by the number of tests N in order to average and reduce the multi-path effect as shown in equation 2.7.

$$\Gamma_{\text{mean}}^{\text{MUT}} = \left(\sum_{\text{i}=1}^{\text{N}} \Gamma_{\text{i}}^{\text{MUT}} \right) /\text{N} \tag{2.7}$$

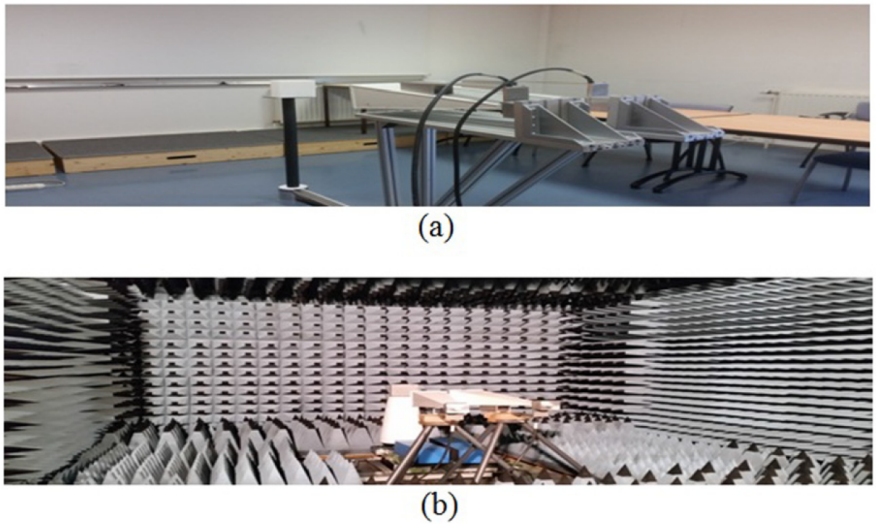

Figure 2.9: Free-space measurement setup in a) a multi-path and b) an anechoic environment [37] (Reused with permission from AIP Publishing).

.

The results of the measured reflection coefficient are compared to reflection coefficient obtained in the anechoic chamber, results without de-embedding and simulation results are shown in Figure 2.10. The results show that the de-embedding method is very effective in removing the multi-path reflections from the environment with the results almost equal to the results obtained in an anechoic environment and the CST simulation.

In order to extract the dielectric constant of the material from the measured reflection coefficient, an extra test is preformed with the same previous step but with material backed by metal. Finally the dielectric constant of the material can be directly calculated using the following set of equations based on the model for TE polarization developed by Fenner et al. in [11].

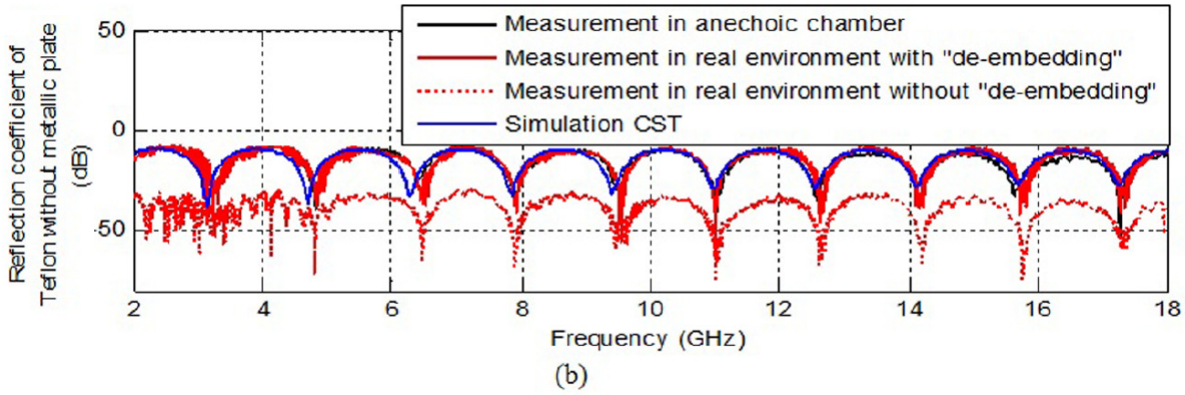

Figure 2.10: Reflection coefficent of teflon sample from different measurments compared with simulation [37] (Reused with permission from AIP Publishing).

.

$$\varepsilon_{\mathrm{r}} = \frac{\mathrm{Z}_0^2}{\mathrm{Z}^2} + \sin^2 \Phi_0 - \quad \text{TE polarization} \tag{2.8}$$

Where

$$Z^2 = \frac{Z_0 Z^A Z^B}{Z_0 + Z^A - Z^B} \tag{2.9}$$

$$Z^A = Z_0 \left(\frac{1 + \Gamma^{\mathrm{MUT-MP}}}{1 - \Gamma^{\mathrm{MUT-MP}}} \right) \tag{2.10}$$

$$Z^B = Z_0 \left(\frac{1 + \Gamma^{\mathrm{MUT}}}{1 - \Gamma^{\mathrm{MUT}}} \right) \tag{2.11}$$

Where Z_0 and Z^2 represent the wave impedance of free space and transverse impedance respectively, while Z^A and Z^B represent the wave impedance of the sample in the case of material backed by metal (MUT-MP) and material only (MUT). Moreover, Φ_0 is the wave incidence angle.

The resulting epsilon over the bandwidth from 2 to 18 GHz compared to the result obtained inside the anechoic chamber, from a coaxial and waveguide probe and value reported in datasheet is shown in Figure 2.11:

This method is proven to be effective in reducing the multipath reflections from the environment. However, it requires an expensive VNA and bulky horn antennas and is not able to extract the loss tangent or the thickness of the material.

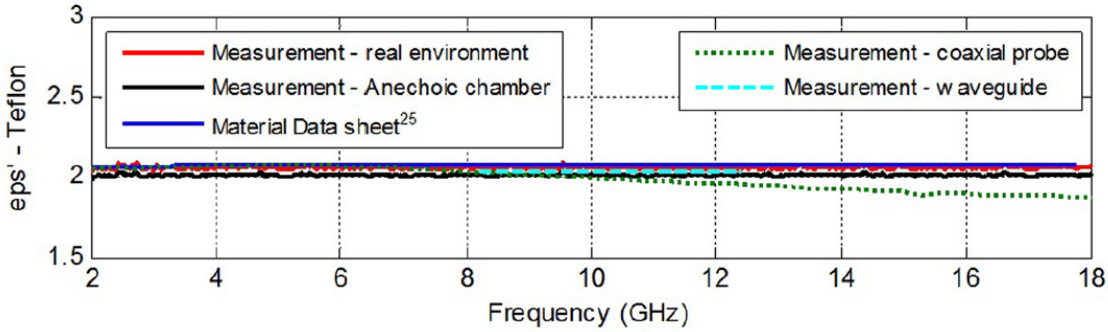

Figure 2.11: Extracted dielectric constant of Teflon sample from different methods compared with the datasheet [37] (Reused with permission from AIP Publishing).

In [9], the authors propose another free-space technique using a signal generator with an oscilloscope instead of the VNA. This method utilizes the Radar Cross Section (RCS) characteristics of the material for calculating its dielectric properties. The setup consists of a pulse signal generator connected to the Tx antenna and synchronized through a trigger with an oscilloscope connected to Rx antenna for sampling the received signal.

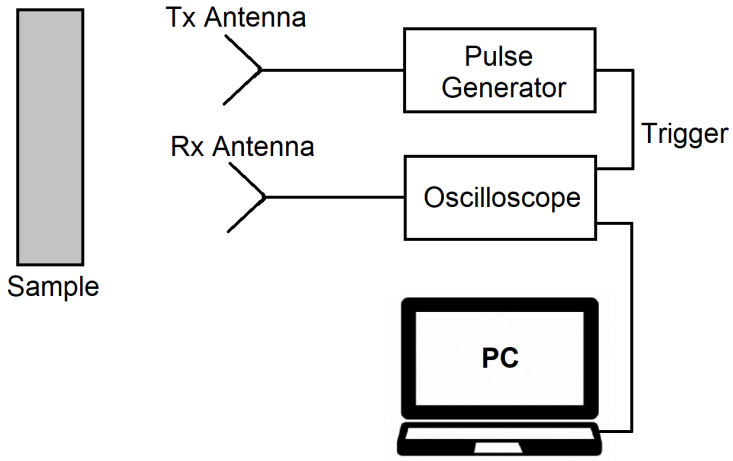

Figure 2.12: Measurement setup for the RCS based method in [9].

The material sample is located 1 m away from the two Vivaldi antennas which are placed side by side in quasi-monostatic configuration. The principle used for calculating the dielectric constant and loss tangent of the material depend on the time-domain reflected

pulse characteristics for the target (Material Sample). Those reflected pulse characteristics can be used to calculate the RCS of the target, which is related to the reflection coefficient of the target material according to equation 2.12.

$$\sigma_{\mathrm{MUT}} = \sigma_{\infty} \left| \Gamma^2_{\mathrm{MUT}} \right| \tag{2.12}$$

Where σ_{MUT} and σ_{∞} represent the RCS for the material and its metallic equivalent respectively. The RCS in both cases can be calculated using the following equation:

$$\sigma_{\mathrm{avg}} = \frac{\int_{-\infty}^{\infty} |r(t)|^2 dt}{\int_{-\infty}^{\infty} |s(t)|^2 dt} \cdot \frac{\left(4\pi R^2\right)^2}{h_{et} \cdot h_{er}} \tag{2.13}$$

Where $r(t)$ is the received pulse reflected from the material in time domain, and $s(t)$ is the transmitted pulse also in time domain. Figure 2.13 shows the transmitted pulse $s(t)$ along with the recieved pulse $r(t)$ for the case of ambient, metal and Granite sample. The distance to the target is expressed by R while h_{et} and h_{er} are the heights of the Tx and Rx antennas respectively. After measuring the RCS of the material and its metallic equivalent, then Γ_{MUT} can then be calculated and eventually the dielectric constant can be obtained using equation 2.14.

$$\varepsilon_r = \left(\frac{1 - \Gamma_{\mathrm{MUT}}}{1 + \Gamma_{\mathrm{MUT}}} \right)^2 \tag{2.14}$$

In this case, the incidence angle is assumed to be zero (normal) to simplify the calculations. However, equation 2.15 is a more general formula taking incidence angle θ_i into account. This equation holds for perpendicular (horizontal) polarization only, which is the polarization of the used Vivaldi antennas.

$$\Gamma_{\perp} = \frac{\cos\theta_i - \sqrt{\varepsilon_2/\varepsilon_1 - \sin^2\theta_i}}{\cos\theta_i + \sqrt{\varepsilon_2/\varepsilon_1 - \sin^2\theta_i}} \tag{2.15}$$

The main advantage of this method is that it does not require a planar or especially shaped material samples compared to other reported methods. The utilization of the target RCS means that any arbitrarily shaped material can be characterized using this technique. However, it requires a pulse signal generator along with an oscilloscope in order to generate and resolve the pulses from the target.

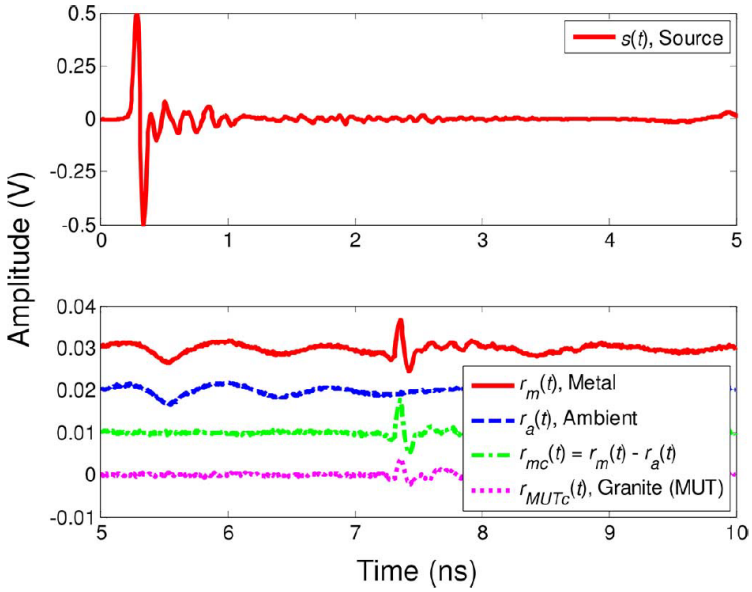

Figure 2.13: Transmitted and received pulse signals from a granite slab [9] (© 2015 IEEE).

The authors also proposed a modified method for extracting the dielectric constant and loss tangent as a function of frequency. Figure 2.14 shows the extracted dielectric constant and loss tangent for a granite slab using this method, and compared to the same parameters extracted using Agilent probe. The results show a good agreement for the extraction of the real part of the dielectric constant. However, deviation in the loss tangent data is obvious.

Another interesting free-space technique was reported in [6] and [7]. The researchers proposed a material characterization system using Ultra Wide Band UWB Frequency Modulated Continuous Wave FMCW radar with 50 GHz bandwidth using the setup shown in Figure 2.15.

The purpose of this technique is first extracting the reflection coefficient of the material from the FMCW real-only baseband signal and consecutively estimating the dielectric constant from it. Before starting the measurement, a traditional calibration or de-embedding steps are done in order to eliminate the effect of the channels and antennas and bring the measurement reference plane to the surface of the material. This is the same principle used in VNA calibration. The extracted reflection coefficient over the frequency band of the radar is then fitted to the Fresnel reflection factor equation using Gauss-Newton algorithm to extract the dielectric constant and the loss tangent of the material.

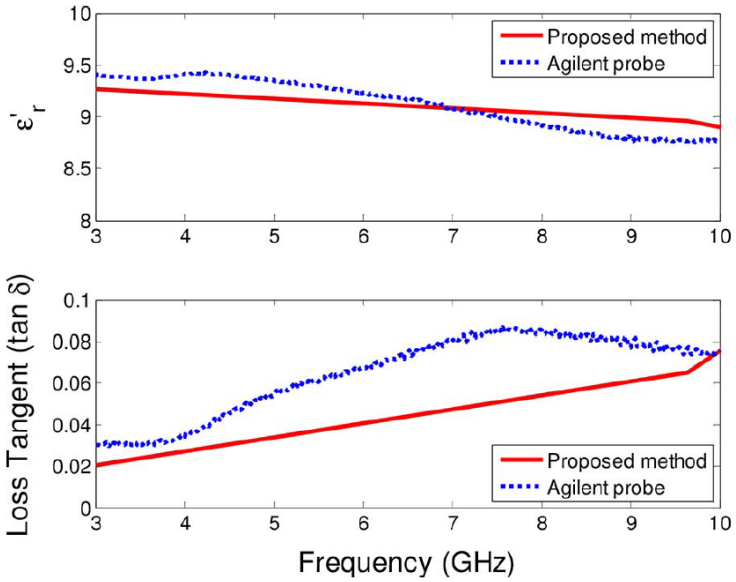

Figure 2.14: Extracted dielctric constant and loss tangent for a granite slab [9] (© 2015 IEEE).

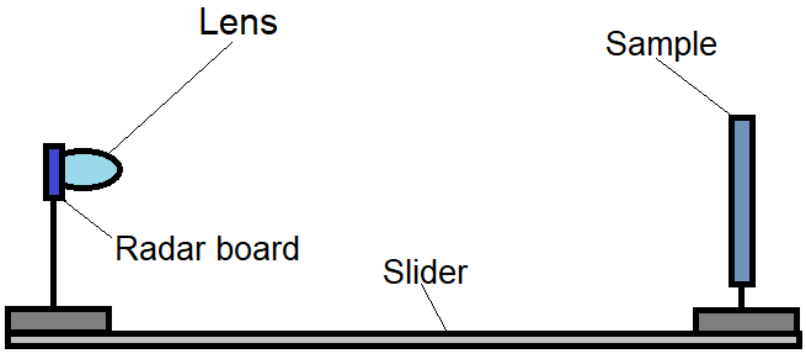

Figure 2.15: Material characterization test setup used in [6]

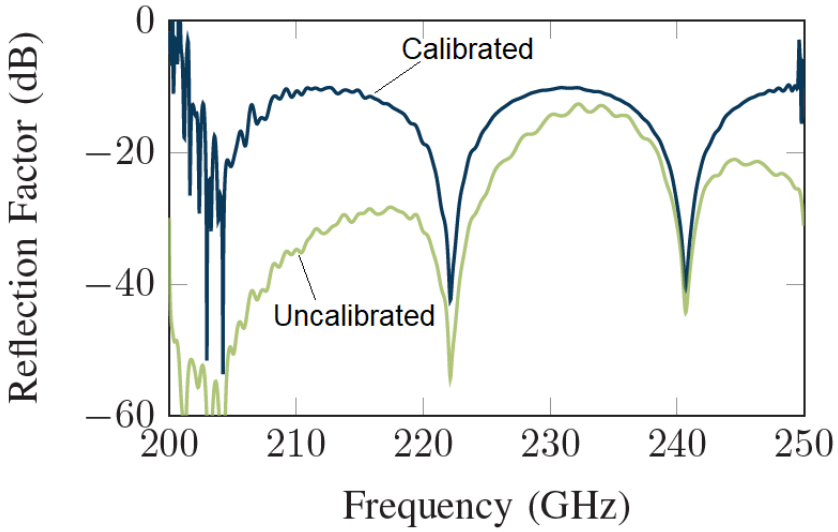

Figure 2.16: Calibrated and uncalibrated reflection coefficient extracted using FMCW radar for a PTFE sample [6] (© 2017 IEEE).

This method uses a custom designed UWB radar chip with 50 GHz BW and utilizes the real only data from the radar baseband. Also due to the high frequency band used (200GHz to 250 GHz), the measurement range is relatively shorter than other lower frequency systems. There are other material characterization systems that use parallel plates with the material between them to monitor the change in capacitance according to the change in material permittivity. However, these systems are more suitable for low frequency measurements and for thin sheet samples. The strengths of each technique are summarized in Figure 2.17.

Finally, a comparison between all the discussed methods with respect to the frequency band used and the tested material loss is shown in Figure 2.18

2.5 Summary

In this chapter, several material characterization methods were discussed and compared. Resonance methods are very accurate and work well for low loss materials. However, it requires direct contact with the material sample and needs a very accurate VNA. One-port method is broadband and suitable for lossy materials. It also works well with liquid

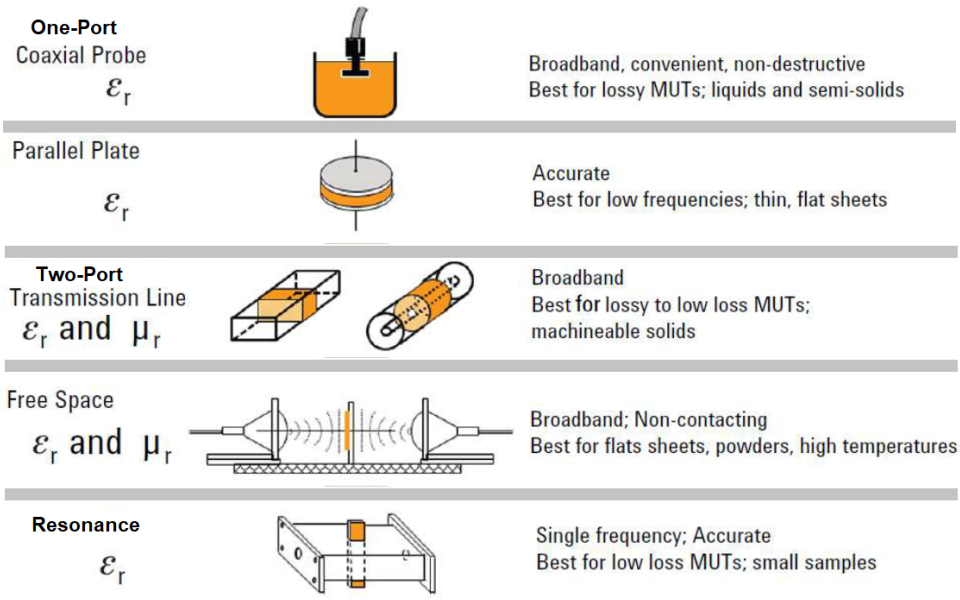

Figure 2.17: Comparison between different material characterization techniques according to their strengths (© Agilent Technologies) [27].

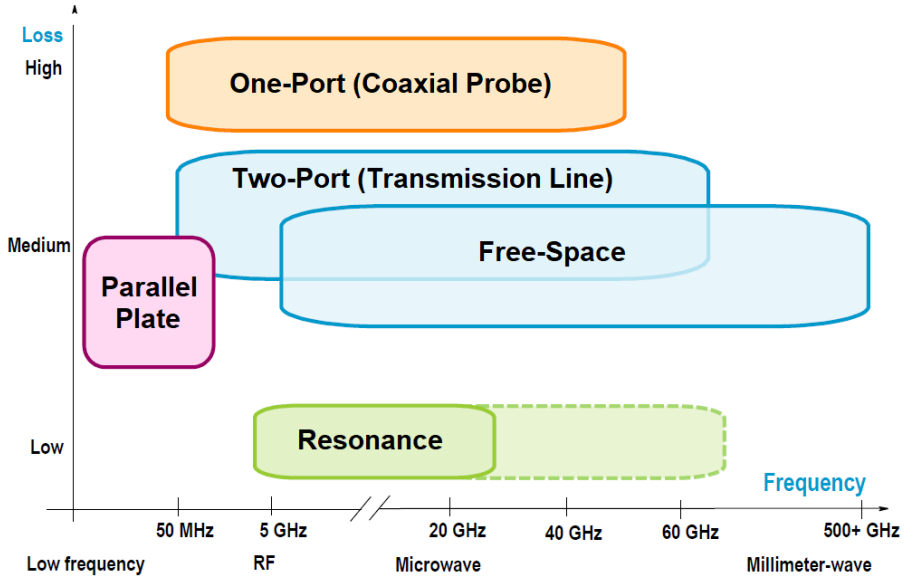

Figure 2.18: Comparison between different material characterization techniques according to frequency range and material loss (© Agilent Technologies) [27].

samples and does not require special machining for the solid materials. In contrast, two-port methods require a machined solid sample to fit inside the waveguide. Both one-port and two-port methods need a direct contact with the samples and depend on a bulky and expensive VNA for measurements. Free-space method does not require any contact or shaping for the sample which makes it ideal for some applications where direct contact with the material is not possible or poses a risk to the measurement equipment.

Different techniques for the Free-space method were discussed. The first technique proposes a solution for the multipath reflections when the measurement is done outside an anechoic environment. The second technique introduces a method for characterizing samples with arbitrary shapes based on the RCS of the material. Finally, a UWB radar based technique was discussed which uses FMCW real-only baseband information to extract dielectric properties of the material instead of using an expensive VNA. In conclusion, it was evident that a solution which overcomes most of the drawbacks of these methods is needed. Such a system would dispense with the need for a VNA or expensive lab equipment. It should also be non-contact and non-destructive and suitable for multi-path environments. In our literature, we propose such a system using a complex baseband FMCW radar that can accurately characterize all kinds of materials and identify the layer configuration using both magnitude and phase information. Our system is compact, mobile and low-cost which makes it ideal for many applications.

Chapter 3

System Model and Analysis

In the previous chapter, a comprehensive discussion about material characterization methods was introduced. It was obvious that most of these methods are either reliant on expensive equipment or require a direct contact or special shaping for the sample. The FMCW technique in [6] required a custom radar design with 50GHz bandwidth [42] and does not utilize the complex baseband information from the radar. We propose a free-space system that uses a commercial 77GHz FMCW radar chip with 4GHz bandwidth, widely used in the automotive industry, to accurately and reliably characterize materials in a non-contact and non-invasisve way. The used board has a complex IQ baseband providing both magnitude and phase information about the reflected signal from the target. In this chapter, we will investigate our system model in-depth and provide analysis and simulation results to verify our theoretical models. The importance of using the phase information for enhancing the measurement accuracy and identifying the layer configuration is discussed. Finally, the methods for extracting the dielectric parameters from the radar complex baseband information are introduced.

3.1 Problem Modeling

In order to extract the dielectric parameters of a material sample, the first step is to accurately extract the reflection coefficient at the surface of the material. In this section, we are modeling the material sample as a flat dielectric slab with finite thickness with the aim of extracting the input reflection coefficient at its surface ($z = -d$). For simplicity, we are assuming that the sample is suspended in air. However, our models can be easily modified to assume a metal substrate or even a 2nd dielectric layer. Additionally, we

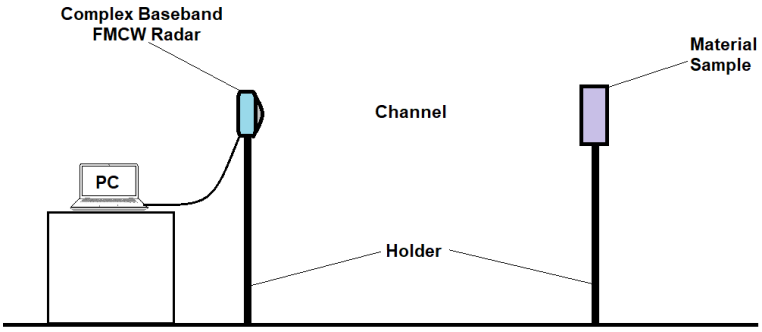

Figure 3.1: Proposed material characterization setup.

assume a constant dielectric constant ϵ_r and loss tangent tan δ for the entire band of interest in all our models.

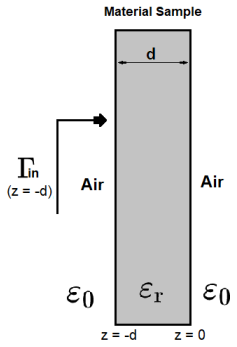

Figure 3.2: Model for flat dielectric slab with finite thickness backed by air.

Two theoretical models are discussed for the flat dielectric slab assumption. The first model is derived using transmission line theory for modeling the material and the next layer as a transmission line with a characteristic impedance Z_{01} and electric length γ d where γ is the propagation constant and d is the slab thickness. The second model is the multiple reflections model which accounts for the multiple reflections and transmissions inside the material sample. Finally, an FMCW model taking into account the radar waveform and the channel delay is introduced. This model is essential for demonstrating how the complex reflection coefficient is related to the complex baseband of FMCW radar.

3.1.1 Transmission Line Model

In the transmission line model, the dielectric slab is modeled as a lossy transmission line terminated by a load representing the backing layer. The dielectric slab is assumed to be surrounded by air on both sides, and the characteristic impedance of the air before and after the dielectric slab are represented by Z_0 and Z_{L} while the characteristic impedance of the dielectric slab is Z_{01}. These characteristic impedances are equivalent to the wave impedances of the air and the dielectric layer.

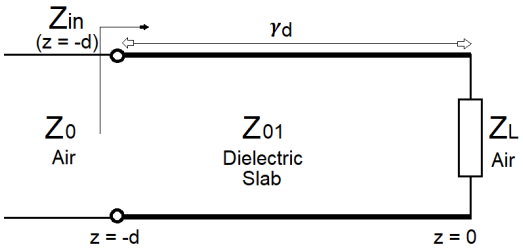

Figure 3.3: Transmission line model for flat dielectric slab with finite thickness backed by air.

The characteristic impedance Z_0 representing the air before the dielectric slab is almost equal to free space impedance which is valued 376.7 ohms. The characteristic impedance of the dielectric slab is a function of the complex permittivity of the slab material as shown in equation 3.1 from [11].

$$Z_{01} = Z_0 \cdot \sqrt{\frac{1}{\varepsilon_r}} \tag{3.1}$$

The input impedance Z_{in} of the equivalent transmission line can then be calculated as shown in equation 3.2 from [38].

$$Z_{in}(z = -d) = Z_{01}\left[\frac{Z_L + Z_{01} \cdot \tanh(\gamma d)}{Z_{01} + Z_L \cdot \tanh(\gamma d)}\right] \tag{3.2}$$

Where γ is the propagation constant and d is the slab thickness. Finally, the input reflection coefficient can be easily calculated using the reflection coefficient formula as seen in equation 3.3 from [38].

$$\Gamma_{in} = \frac{Z_{in} - Z_0}{Z_{in} + Z_0} \tag{3.3}$$

This input reflection coefficient Γ_{in} represents the reflection coefficient seen at the surface of the dielectric slab ($z = -d$) which contains the information needed to extract the dielectric parameters for the slab material.

This equation can then be used to simulate the model using the dielectric constant ϵ_r, the loss tangent tan δ and the thickness d of the slab as inputs. Figure 3.4 below shows the simulation results for the input reflection coefficient's magnitude and phase of a Teflon slab ($\epsilon_r = 2.07, tan\,\delta = 0.0001$) with a thickness of 5mm over a bandwidth from 10 to 100 GHz.

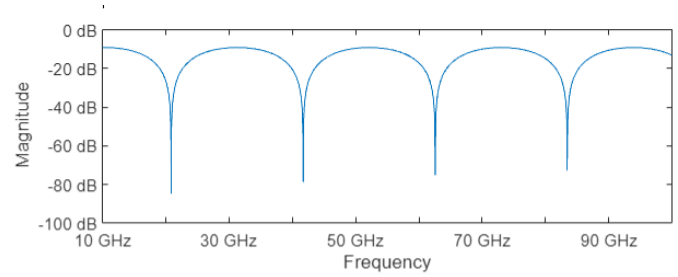

(a) Magnitude

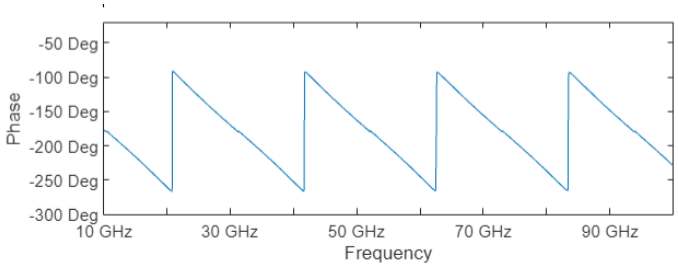

(b) Phase (Unwrapped)

Figure 3.4: The magnitude and the unwrapped phase of Γ_{in} for a 5mm thick Teflon sample using the transmission line model.

This model is simple and can be easily extended to multi-layer dielectrics as sown in Figure 3.5, by using the Z_{in} of the transmission line as a load impedance for the previous layer as shown in the following figures and set of equations.

$$Z_{01} = Z_0 \cdot \sqrt{\frac{1}{\varepsilon_{r1}}} \tag{3.4}$$

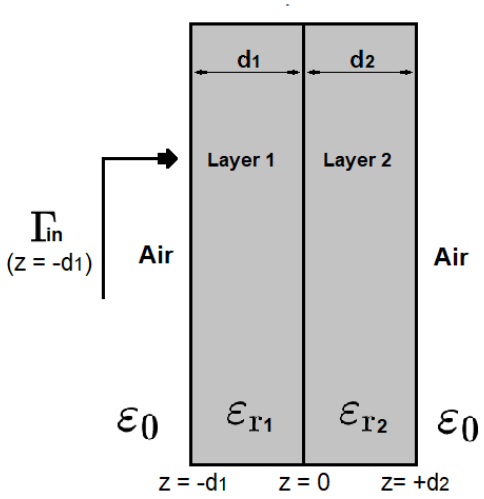

Figure 3.5: Model for multi-layer flat dielectric slab with finite thickness backed by air.

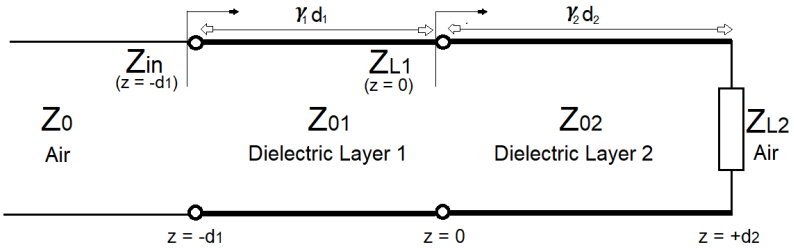

Figure 3.6: Transmission line model for multi-layer flat dielectric slab with finite thickness surrounded by air.

$$Z_{02} = Z_0 \cdot \sqrt{\frac{1}{\varepsilon_{r2}}} \tag{3.5}$$

$$Z_{L1}(z=0) = Z_{02}\left[\frac{Z_{L2} + Z_{02} \cdot \tanh(\gamma_2 d_2)}{Z_{02} + Z_{L2} \cdot \tanh(\gamma_2 d_2)}\right] \tag{3.6}$$

$$Z_{in}(z=-d_1) = Z_{01}\left[\frac{Z_{L1} + Z_{01} \cdot \tanh(\gamma_1 d_1)}{Z_{01} + Z_{L1} \cdot \tanh(\gamma_1 d_1)}\right] \tag{3.7}$$

$$\Gamma_{in} = \frac{Z_{in} - Z_0}{Z_{in} + Z_0} \tag{3.8}$$

Figure 3.7 shows the magnitude and phase of Γ_{in} for the 5mm Teflon slab backed by a 1mm Acrylic layer and then by air. The layer thicknesses are chosen so that we have obvious disturbance on the magnitude and phase caused by the second layer reflections. It is obvious that the magnitude and phase are changed compared to Figure 3.4 due to the extra reflection components added by the Acrylic layer.

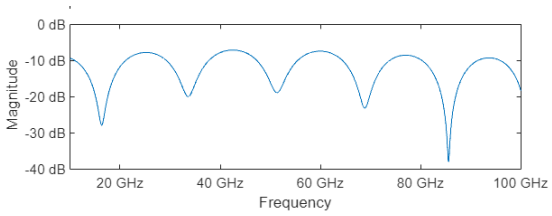

(a) Magnitude

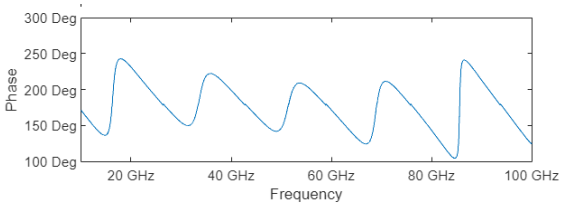

(b) Phase (Unwrapped)

Figure 3.7: The simulated magnitude and the unwrapped phase of Γ_{in} for Teflon-Acrylic dielectric slab backed by air using the transmission line model.

3.1.2 Multiple Reflections Model

The second model used for modeling the dielectric slab with a finite thickness ($\theta = \gamma d$), is the multiple reflections model which is similar to FP interferometer method commonly used in photonics. In this model, all reflections happening internally between the two sides of the slab due to an incident wave are considered. The incident wave is assumed to be a plane wave normal to the surface of the slab with a normalized amplitude of one. Upon the wave incidence on the slab surface, part of the incident wave is reflected due to the contrast between air with a relative permittivity ≈ 1 and the dielectric material with a relative permittivity ε_r as shown in figure 3.8.

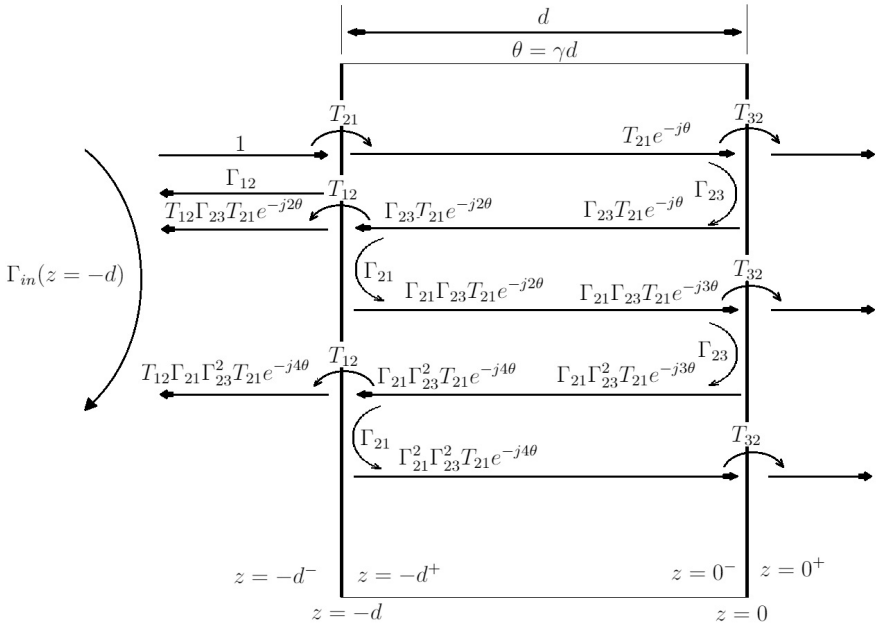

Figure 3.8: Transmissions and reflections inside a dielectric slab with finite thickness.

The reflected portion at this first incidence, expressed as Γ_{12} is dependent on the dielectric constant of the material as shown in equation 3.9 from [11].

$$\Gamma_{12} = \frac{1 - \sqrt{\varepsilon_r}}{1 + \sqrt{\varepsilon_r}} \tag{3.9}$$

The transmitted part of the wave, expressed as $T_{21} = 1 + \Gamma_{12}$, is then transmitted through the slab to the other interface and affected by the propagation constant γ. The

reflection and transmission are repeated indefinitely between the two interfaces. The input reflection coefficient at the surface of the slab is the summation of all the reflection and transmission components seen at the first interface ($z = -d$) as seen in equation 3.10 and 3.11. Finally, equation 3.14 represents the closed form for that summation [5].

$$\Gamma_{\text{in}}\ (z = -d) = \Gamma_{12} + T_{12}\Gamma_{23}T_{21}e^{-2\theta} + T_{12}\Gamma_{21}\Gamma_{23}^2T_{21}e^{-4\theta} + \dots \tag{3.10}$$

$$\Gamma_{\text{in}}\,(z = -d) = \Gamma_{12} + T_{12}\Gamma_{23}T_{21}e^{-2\theta}\left[1 + \Gamma_{21}\Gamma_{23}e^{-2\theta} + \left(\Gamma_{21}\Gamma_{23}e^{-2\theta}\right)^2 + \dots\right] \tag{3.11}$$

$$\Gamma_{\text{in}}\ (z = -d) = \frac{\Gamma_{12} + \Gamma_{23}e^{-2\gamma d}}{1 + \Gamma_{12}\Gamma_{23}e^{-2\gamma d}} \tag{3.12}$$

$$\Gamma_{23} = -\Gamma_{12} \tag{3.13}$$

$$\Gamma_{\text{in}}\ (z = -d) = \frac{\Gamma_{12}(1 - e^{-2\gamma d})}{1 - \Gamma_{12}^2e^{-2\gamma d}} \tag{3.14}$$

Where

$$\gamma = \alpha + j\beta \tag{3.15}$$

$$\beta = \frac{2\pi\sqrt{\varepsilon_r}}{\lambda} \tag{3.16}$$

$$\alpha = \frac{\pi\sqrt{\varepsilon_r}}{\lambda}\tan\delta \tag{3.17}$$

While β is the phase constnat, α represents the attenuation constant and λ is the free-space wavelength. Figure 3.9 shows the MATLAB simulation results for the magnitude and phase of Γ_{in} for a 5mm Teflon slab extracted using this model and compared with the transmission line model. The simulation results show a perfect agreement between the two models. However, the transmission line model is easier for multi-layer extension.

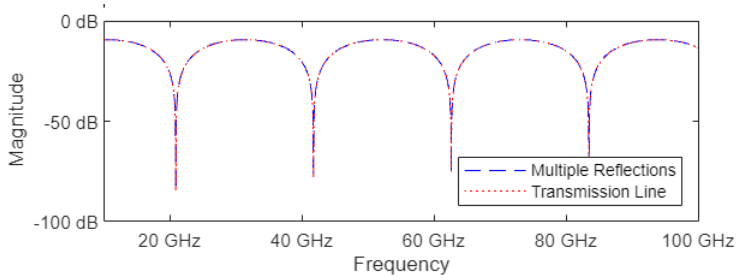

(a) Magnitude

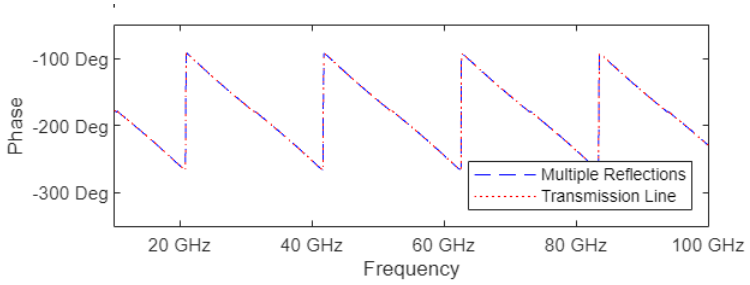

(b) Phase (Unwrapped)

Figure 3.9: A comparison between the magnitude and the unwrapped phase of Γ_{in} from the multiple reflections and the transmission line models for a 5mm teflon slab backed by air.

3.1.3 FMCW Model

After introducing the input reflection coefficient models in the previous section, another model is needed for extracting the input reflection coefficient from the complex baseband of the FMCW radar. In this section, an introduction about FMCW theory is presented along with derivations for the complex baseband formulas and discussion on the equivalency of the complex baseband information and the complex input reflection coefficient of the dielectric slab. A more detailed discussion regarding the FMCW radar board used for the measurement is introduced in Chapter 4. FMCW radar is a special type of radar which uses a frequency modulated waveform for measuring the range of the target. This modulating waveform is usually a periodic linear or sawtooth waveform that drives a Voltage Controlled Oscillator VCO for generating what is called a *Chirp* signal.

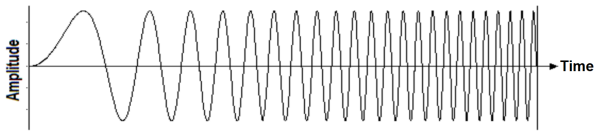

Figure 3.10: Chirp Waveform [17]

This chirp signal is then transmitted towards the target and reflected back to the receiver after a specific duration that is proportional to the range of the target. The received chirp is then mixed with the conjugate of the transmitted chirp, lowpass filtered and finally converted to frequency domain through Fast Fourier Transform FFT to produce the baseband signal also known as *Beat* signal.

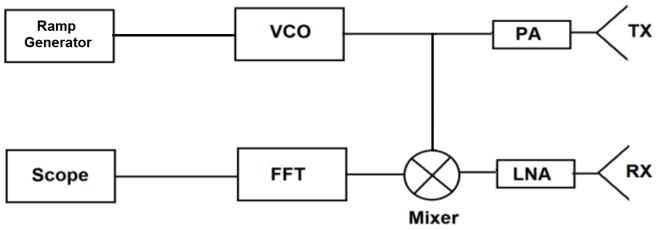

Figure 3.11: Block diagram of FMCW radar [17]

Due to the time shift between the received and transmitted chirps, the beat signal resulting from the mixing of the two chirps will have a frequency that is directly proportional to the time delay between transmitting and receiving the chirp. This simply means that

the frequency of the beat signal is directly proportional to the range of the target as shown in equation 3.18.

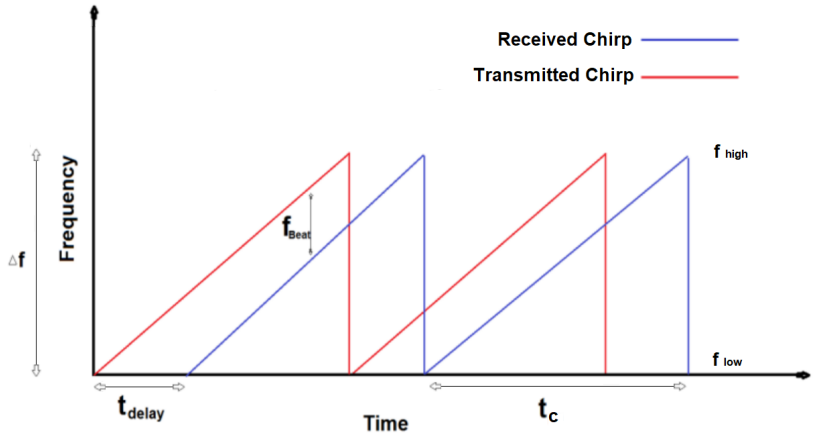

Figure 3.12: Transmissions and reflections inside a dielectric slab with finite thickness [17]

$$f_{\text{beat}} = \frac{2BR}{t_c c} \tag{3.18}$$

Where f_{beat} is the frequency of the baseband beat signal, B is the chirp bandwidth, R is the target range, t_c the period of the transmitted chirp and c is the speed of light. In order to formulate the FMCW model and relate it to Γ_{in} model, we first need to formulate the Γ_{in} model in time-domain. The Γ_{in} model that best describes what happens in reality and the model that is more relevant to the transmission and reflection behaviour of the chirp signal, is the Multiple Reflections model.

Starting from equation 3.10, and assuming a lossy dielectric material, the slab thickness expressed as $\theta = \gamma d$, can also be represented as $\omega C_1 + j\omega C_2$ as seen in equation 3.21, where C_1 and C_2 represent the constant terms as shown in equation 3.22 and 3.23.

$$\theta = \gamma d = (\alpha + j\beta)\, d = \left(\frac{\pi\sqrt{\varepsilon_r}}{\lambda} tan\delta + j\frac{2\pi\sqrt{\varepsilon_r}}{\lambda} \right) d \tag{3.19}$$

$$= \frac{\pi\sqrt{\varepsilon_r} tan\delta}{\lambda} d + j\frac{2\pi\sqrt{\varepsilon_r}}{\lambda} d = \frac{\omega\sqrt{\varepsilon_r} tan\delta}{2c} d + j\frac{\omega\sqrt{\varepsilon_r}}{c} d \tag{3.20}$$

$$= \omega C_1 + j\omega C_2 \tag{3.21}$$

where

$$C_1 = \frac{\sqrt{\varepsilon_r} tan\delta}{2c} d, \tag{3.22}$$

$$C_2 = \frac{\sqrt{\varepsilon_r}}{c} d \tag{3.23}$$

As a result, equation 3.10 can then be represented as a function of frequency ω as shown in equation 3.24 (Assuming no chromatic dispersion due to limited bandwidth of the radar).

$$\Gamma_{\text{in}}(\omega) = \Gamma_{12} + T_{12}\Gamma_{23}T_{21}e^{-2\omega C_1}e^{-j2\omega C_2} + T_{12}\Gamma_{21}\Gamma_{23}^2 T_{21}e^{-4\omega C_1}e^{-j4\omega C_2} + \ldots \tag{3.24}$$

For simplicity, we are representing the constant reflection and transmission terms as a_0,a_1,a_2....

$$\Gamma_{\text{in}}(\omega) = a_0 + a_1 e^{-2\omega C_1}e^{-j2\omega C_2} + a_2 e^{-4\omega C_1}e^{-j4\omega C_2} + \ldots \tag{3.25}$$

This equation is rewritten to reach the simpler expression in 3.26.

$$\Gamma_{in}(\omega) = \sum_{n=0}^{\infty} a_n e^{-2n\omega C_1}e^{-j2n\omega C_2} \tag{3.26}$$

The complex chirp signal $x(t)$ generated by the FMCW radar with amplitude A_0 and initial phase θ_0 as shown in equation 3.27, is transmitted from the radar towards the target, reaching it after a duration $\tau/2$ as $x'(t)$ (The time delay $\tau/2$ is resulting from the distance to target R). In equation 3.27 , $\omega(t)$ represents the linear frequency variation in the chirp starting from an initial frequency ω_0 with a slope equal to B/t_c as seen in equation 3.29, where B is the chirp bandwidth and t_c is the chirp duration. This equation also represents the relationship between the time t and the frequency of the chirp $\omega(t)$.

$$x(t) = A_0 e^{j(\omega(t)t + \theta_0)} \tag{3.27}$$

Where

$$\tau = \frac{2R}{c} \tag{3.28}$$

$$\omega(t) = \omega_0 + \frac{B}{t_c}t \tag{3.29}$$

Due to the equivalency between the frequency and the time of the chirp, the time domain chirp equation $x(t)$ can be expressed entirely in frequency domain using the relationship between frequency and time shown in equation 3.29. The resulting frequency domain chirp is presented in equation 3.30.

$$x(\omega) = A_0 e^{j(\omega^2 \frac{t_c}{B} - \omega\omega_0 \frac{t_c}{B} + \theta_0)} \tag{3.30}$$

The chirp is then delayed by a duration $\tau/2$ resulting from the path between the radar and the material.

$$x'(\omega) = x(\omega).e^{-j\omega\frac{\tau}{2}} = A_0 e^{j(\omega(t)^2 \frac{t_c}{B} - \omega(t)\omega_0 \frac{t_c}{B} - \omega\frac{\tau}{2} + \theta_0)} \tag{3.31}$$

The delayed chirp $x'(\omega)$ is then multiplied by the input reflection coefficient of the material $\Gamma_{in}(\omega)$ generating $y(\omega)$ as seen in equation 3.33. This $y(\omega)$ signal exhibits another path delay $\tau/2$ resulting from the return path from the material to the radar, before being received by the radar as $y'(\omega)$ as shown in equation 3.34.

$$y(\omega) = x'(\omega).\Gamma_{in}(\omega) = \left(A_0 e^{j(\omega(t)^2 \frac{t_c}{B} - \omega(t)\omega_0 \frac{t_c}{B} - \omega\frac{\tau}{2} + \theta_0)}\right) . \left(\sum_{n=0}^{\infty} a_n e^{-2n\omega C_1} e^{-j2n\omega C_2}\right) \tag{3.32}$$

$$y(\omega) = A_0 \sum_{n=0}^{\infty} a_n e^{-2n\omega C_1} e^{-j(2n\omega C_2 - \omega(t)^2 \frac{t_c}{B} + \omega(t)\omega_0 \frac{t_c}{B} + \omega\frac{\tau}{2} - \theta_0)} \tag{3.33}$$

$$y'(\omega) = y(\omega).e^{-j\omega\frac{\tau}{2}} = A_0 \sum_{n=0}^{\infty} a_n e^{-2n\omega C_1} e^{-j(2n\omega C_2 - \omega(t)^2 \frac{t_c}{B} + \omega(t)\omega_0 \frac{t_c}{B} + \omega\tau - \theta_0)} \tag{3.34}$$

It is worth mentioning that due to the small wave travelling time inside the material, compared to the chirp duration, the frequency of the multiple reflection components can

be assumed to be almost constant. To study this frequency shift effect, we first derive a formula for the time difference t_d, due to the wave travelling between the two interfaces of the sample, as presented in equation 3.35.

$$t_d = \frac{2nd\sqrt{\varepsilon_r}}{c} \tag{3.35}$$

where n is the order of the reflection term. Using equation 3.29, the frequency difference of the chirp corresponding to this duration is presented in equation 3.36.

$$\Delta\omega = \frac{B}{t_c} t_d \tag{3.36}$$

In our case, the first reflection term has a frequency difference of 23.8 KHz which correspond to a frequency error of 0.0005 % when compared to the 4.41 GHz sweeping bandwidth of the radar. In practice, and according to our simulations, the first 4 reflection terms are the main contributing terms in the input reflection coefficient, while the remaining terms are very small and can be neglected.

Finally, the received signal by the FMCW radar is mixed with the conjugate of the transmitted chirp $x(\omega)$ to generate the baseband signal $z(\omega)$ as seen in equation 3.37.

$$z(\omega) = y'(\omega).\overline{x(\omega)} = \left(A_0 \sum_{n=0}^{\infty} a_n e^{-2n\omega C_1} e^{-j(2n\omega C_2 - \omega(t)^2 \frac{t_c}{B} + \omega(t)\omega_0 \frac{t_c}{B} + \omega\tau - \theta_0)} \right) . \left(A_0 e^{-j(\omega(t)^2 \frac{t_c}{B} - \omega(t)\omega_0 \frac{t_c}{B} + \theta_0)} \right) \tag{3.37}$$

$$z(\omega) = A_0^2 \sum_{n=0}^{\infty} a_n e^{-2n\omega C_1} e^{-j(2n\omega C_2 - \omega(t)^2 \frac{t_c}{B} + \omega(t)\omega_0 \frac{t_c}{B} + \omega\tau - \theta_0 + \omega(t)^2 \frac{t_c}{B} - \omega(t)\omega_0 \frac{t_c}{B} + \theta_0)} \tag{3.38}$$

The phase factors $\omega(t)^2 t_c/B$, $\omega(t)\omega_0 t_c/B$ and the initial phase term θ_0 from the two signals cancel out, resulting in equation 3.39

$$z(\omega) = A_0^2 \sum_{n=0}^{\infty} a_n e^{-2n\omega C_1} e^{-j(2n\omega C_2 + \omega\tau)} \tag{3.39}$$

In comparison with $\Gamma_{in}(\omega)$ formula in equation 3.26, it is obvious that the baseband signal $z(\omega)$ contains the magnitude of $\Gamma_{in}(\omega)$ scaled by A_0^2. Additionally, the phase of the

FMCW baseband signal is similar to the phase of Γ_{in} with the additional linear phase distortion term $\omega\tau$. This linear phase distortion is resulting from the channel path from the radar to the material and from the material back to the radar. It is also worth noting that in reality, the received signal $y'(t)$ will also be affected by the Tx and Rx antenna gain, the channel path loss and the target RCS, which would also appear at the complex baseband of the radar. Moreover, the real exponential term $e^{-2n\omega C_1}$ is responsible for the attenuation resulting from the losses in the material, and is equal to one in the case of a lossless material.

In order to compare this model with the earlier discussed transmission line model 3.1.1 and multiple reflections model 3.1.2, the FMCW model is simulated using MATLAB. This simulation model is simply the Multiple Reflection model with the complex chirp used as an incident signal. The multiple reflections and transmissions inside the material slab seen in equation 3.10, are considered up to the first 10 terms. Those 10 terms are enough to represent the input reflection coefficient Γ_{in} as all the subsequent terms have a very small contribution and can be neglected. The simulation results for this model are presented in Figure 3.13 with a comparison between the FMCW model and Multiple Reflections model. Due to the limited memory of the machine and the maximum sampling rate that can be used, the simulation was created for a Teflon sample over a small bandwidth of 0 to 10 MHz. In order to have sufficient variations for the magnitude and phase of the FMCW baseband over this small bandwidth, a large theoretical material thickness of 40m was used. The amplitude A_0 of the transmitted chirp $x(t)$ is simulated for values of 0.5V and 0.25V as seen in Figure 3.13(a). The Tx and Rx antenna gain, the path loss and the target RCS are all assumed to be unity for simplifying the comparison. The magnitude comparison shows a difference of 12 dB between each curve which corresponds to A_0^2 scaling, while the phase comparison confirms the linear phase distortion resulting from the term $\omega\tau$.

There is no doubt that a distortion in the phase or the magnitude of the input reflection coefficient Γ_{in} can cause unwanted errors when used for extracting the dielectric properties of the material sample. For this reason, an accurate calibration is required for removing all magnitude and phase distortions. The details of the calibration are discussed in the next section.

3.2 Calibration

As discussed in the previous section, the magnitude and phase of the FMCW complex baseband, seen in equation 3.39, are distorted compared to magnitude and phase of Γ_{in} in equation 3.26. The magnitude is scaled by A_0^2 while the phase has a path delay dependent

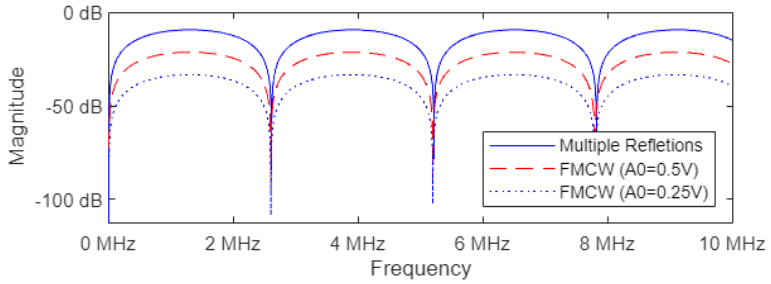

(a) Magnitude

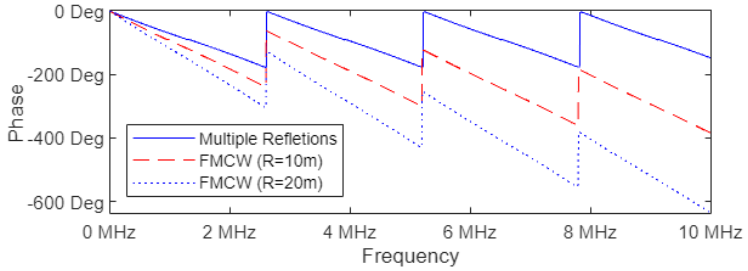

(b) Phase (Unwrapped)

Figure 3.13: A comparison between (a) the magnitude and (b) the unwrapped phase of Γ_{in} from the Multiple Reflections and the FMCW models. The magnitude of the multiple reflection model is compared with the FMCW model for an amplitude A_0 of 0.5V and 0.25V while the phase is compared with FMCW model with target distance R of 10m and 20m.

linear distortion. Additionally, the magnitude will also be affected by the antenna gain of the transmitter and receiver, the path loss and the RCS of the material sample. Fortunately, a system calibration can remove all these magnitude and phase distortions for extracting a clean Γ_{in} from the complex baseband of the FMCW radar. Our setup can be modeled as a one-port network terminated by a load representing the input impedance Z_{in} of the material slab and its backing layer. Additionally, all the magnitude and phase distortions due to the channel, the antennas or the RCS of the material can be modeled by a two-Port error network connected to the load and the measurement system as shown in Figure 3.14.

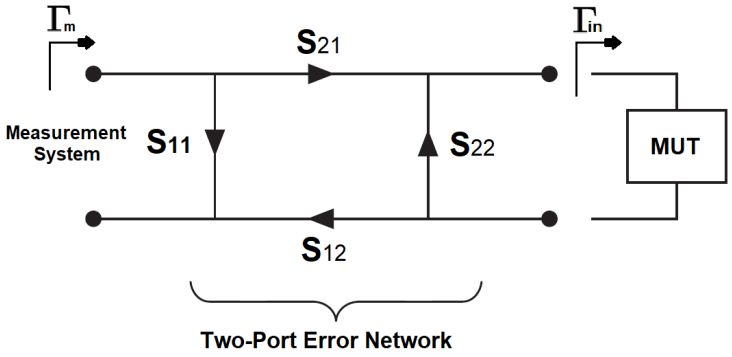

Figure 3.14: Signal flow diagram for the material under test (MUT) with the error network

This model can be considered as an extension to the transmission line model in Figure 3.3 by taking the error effects into consideration. This type of error network is well-known in VNA measurements and can be easily removed using one-Port calibration method [41]. To formulate the calibration technique we should first relate the desired input reflection coefficient Γ_{in} to the measured reflection coefficient Γ_m using the S parameters of the error network as shown in equation 3.40 and 3.41.

$$\Gamma_m = S_{11} + \frac{S_{12}S_{21}\Gamma_{in}}{1 - S_{22}\Gamma_{in}} \tag{3.40}$$

$$\Gamma_{in} = \frac{\Gamma_m - S_{11}}{S_{12}S_{21} + S_{22}\left(\Gamma_m - S_{11}\right)} \tag{3.41}$$

This simply means that in order to extract Γ_{in} of the material, all S parameters of the error network have to be known. The first parameter S_{11} can be measured directly by matching the load for setting Γ_{in} to zero as seen in equation 3.42.

$$\Gamma_{m-match} = S_{11} \tag{3.42}$$

In practice, this means removing the material sample and measuring the reflection coefficient using the measurement system. For simplicity, the product of S_{21} and S_{12} can be considered as one unknown. Therefore, we need two more equations to extract the $S_{12}S_{21}$ product and the S_{22} parameter.

The second equation can be obtained by replacing the material with its metallic equivalent acting as a short circuit termination to the error network. In this case, Γ_{in} will be equal to -1 and the measured reflection coefficient Γ_m will reduce to equation 3.43.

$$\Gamma_{m-short} = S_{11} - \frac{S_{12}S_{21}}{1+S_{22}} = \Gamma_{m-match} - \frac{S_{12}S_{21}}{1+S_{22}} \tag{3.43}$$

The third equation can be be obtained by assuming a shift to the short circuit termination by a known distance Δd which will translate to a phase shift of $2\omega\frac{\Delta d}{c}$. The input reflection coefficient Γ_{in} in this case becomes equal to -$e^{i2\omega\frac{\Delta d}{c}}$ yielding to the third equation 3.44.

$$\Gamma_{m-line} = S_{11} - \frac{S_{12}S_{21}e^{j2\omega\frac{\Delta d}{c}}}{1+S_{22}e^{j2\omega\frac{\Delta d}{c}}} = \Gamma_{m-match} - \frac{S_{12}S_{21}e^{j2\omega\frac{\Delta d}{c}}}{1+S_{22}e^{j2\omega\frac{\Delta d}{c}}} \tag{3.44}$$

By solving those three equations together, all the unknown parameters can be calculated as demonstrated in the following two equations:

$$S_{22} = \frac{(\Gamma_{m-line} - \Gamma_{m-match}) - (\Gamma_{m-short} - \Gamma_{m-match})e^{j2\omega\frac{\Delta d}{c}}}{((\Gamma_{m-short} - \Gamma_{m-match}) - (\Gamma_{m-line} - \Gamma_{m-match}))e^{j2\omega\frac{\Delta d}{c}}} \tag{3.45}$$

$$S_{12}S_{21} = -(\Gamma_{m-short} - \Gamma_{m-match})(1+S_{22}) \tag{3.46}$$

Finally, The input reflection coefficient of the material Γ_{in} can be easily calculated using equation 3.41 as discussed before.

The practical implementation of this calibration technique is presented in chapter 6 with a further discussion about the effect of the calibration errors on the obtained results.

3.3 Extraction of Dielectric Parameters

In the previous sections, we explained the different models for Γ_{in} and how we can extract Γ_{in} after calibrating the complex baseband of FMCW radar. In this section, we will explain how the dielectric properties and the material thickness can be obtained using the extracted Γ_{in}. There are two methods proposed for this purpose, the maxima and minima method and the curve fitting method.

3.3.1 Maxima and Minima Method

According to Γ_{in} models discussed before, and assuming a lossless dielectric material, we can observe the unique periodic behaviour of the magnitude of Γ_{in} resulting from the summation of the multiple reflection components with different phases as shown in equation 3.10. The location of the maxima and minima of the magnitude over the frequency axis and the value of the maxima are specific to the type of the dielectric material and its thickness. This means that those characteristics can be considered as a fingerprint for a certain material with specific thickness.

To derive the relationship between the characteristics of maxima and minima of Γ_{in} magnitude with the dielectric properties of the material, we start with Γ_{in} equation 3.47 for a lossless dielectric material derived from the multiple reflections model.

$$\Gamma_{\text{in}} = \frac{\Gamma_{12}(1 - e^{-j2\beta d})}{1 - \Gamma_{12}^2 e^{-j2\beta d}} \tag{3.47}$$

The maximum value of Γ_{in} magnitude occurs when the term $e^{-i2\beta d}$ in the numerator and denominator of the equation is equal to -1 resulting in equation 3.48.

$$|\Gamma_{in}|_{max} = |\frac{2\Gamma_{12}}{1 + \Gamma_{12}^2}| \tag{3.48}$$

Solving this equation for Γ_{12} results in 2 different values with one of them representing a realistic solution for Γ_{12} which ranges between 0 and -1. The other solution is discarded as it is less than -1. The value of the dielectric constant ε_r can then be calculated from Γ_{12} as shown in equation 3.49.

$$\varepsilon_r = \left(\frac{1 - \Gamma_{12}}{1 + \Gamma_{12}}\right)^2 \tag{3.49}$$

Similarly, the condition at which the magnitude of Γ_{in} is minimum occurs when the term $e^{-i2\beta d}$ is equal to 1 resulting in Γ_{in} to be equal to 0. This particular case occurs when $2\beta d$ is equal to integer multiples of 2π as shown in equation 3.50 where n is the order of the minima.

$$2\beta d = 2n\pi \tag{3.50}$$

A further manipulation to this formula results in equation 3.51 which directly relates the dielectric constant ε_r , the thickness d, and the frequency f where c is the speed of light.

$$\varepsilon_r = \left(\frac{nc}{2fd}\right)^2 \tag{3.51}$$

$$d = \frac{nc}{2f\sqrt{\varepsilon_r}} \tag{3.52}$$

By obtaining the dielectric constant first from the maxima of the magnitude using equation 3.49, the material thickness can then be calculated by knowing the frequency where a minimum is occurring and the order of this minimum. The order can be obtained by dividing the frequency at which the minimum or maximum is occurring by the difference between two subsequent minima or maxima as seen in equation 3.53. This also means that at least one minimum and maximum or two maxima or minima are needed for extracting the thickness using this method.

$$n = \left(\frac{f_{min}}{f_{min(i)} - f_{min(i-1)}}\right) = \left(\frac{f_{max}}{f_{max(i)} - f_{max(i-1)}}\right) \tag{3.53}$$

It is noted that this method works only with lossless dielectric materials. For highly lossy materials, the dielectric constant can be directly obtained from the value of Γ_{12} that the magnitude eventually converges to, by using equation 3.49.

3.3.2 Curve Fitting Method

The second method that can be used for recovering the dielectric properties and thickness of the material for lossy and lossless samples is the non-linear least squares curve fitting method. This method works by finding a solution x_i for the following function :

$$\min\left(\sum |F(x_i) - y_i|^2\right) \tag{3.54}$$

Where $F(x_i)$ represents a nonlinear function while y_i is the data that we are trying to fit. In our case, $F(x_i)$ would be replaced by equation 3.55 for magnitude curve fitting, and equation 3.56 for phase curve fitting, while y_i would be the measured Γ_{in} data of the material sample.

$$|\Gamma_{in}| = \frac{\sqrt{(|\Gamma_{12}| - |\Gamma_{12}|e^{-2\alpha d}\cos 2\beta d)^2 + (|\Gamma_{12}|e^{-2\alpha d}\sin 2\beta d)^2}}{\sqrt{(1 - |\Gamma_{12}|^2 e^{-2\alpha d}\cos 2\beta d)^2 + (|\Gamma_{12}|^2 e^{-2\alpha d}\sin 2\beta d)^2}} \tag{3.55}$$

$$\angle\Gamma_{in} = \tan^{-1}\left(\frac{|\Gamma_{12}|e^{-2\alpha d}\sin 2\beta d}{|\Gamma_{12}|(1 - e^{-2\alpha d}\cos 2\beta d)}\right) - \tan^{-1}\left(\frac{|\Gamma_{12}|^2 e^{-2\alpha d}\sin 2\beta d}{1 - |\Gamma_{12}|^2 e^{-2\alpha d}\cos 2\beta d}\right) \tag{3.56}$$

It is worth mentioning that equation 3.55 and equation 3.56 are the closed form expressions for the magnitude and phase of Γ_{in} obtained from equation 3.14.

This method works for both magnitude and phase of Γ_{in} as both have the same information regarding the dielectric properties and the thickness according to our previous discussion in Section 3.4. This means that we can use the magnitude and phase of Γ_{in} separately for recovering the dielectric constant ε_r , the loss tangent $\tan\delta$ and thickness d of the material sample. For enhancing the accuracy of the curve fitting, we can use the data extracted from the magnitude curve fitting as initial values for the phase curve fitting and vice versa. The curve fitting can be done using curve fitting tool on MATLAB.

3.4 Phase Information and Layer Configuration

In this section, the importance of using the phase information of the input reflection coefficient Γ_{in} is discussed. Most of the reported free-space techniques in Chapter 2 rely on the magnitude information for extracting the dielectric parameters. While the magnitude information is enough for calculating the dielectric constant ε_r, the loss tangent $\tan\delta$ and the thickness d, the same information can also be found from the phase. According to equation 3.56 which represents the phase of Γ_{in} from equation 3.14, the phase has a relationship with the dielectric constant ε_r contained in Γ_{12}, α and β while the loss tangent $\tan\delta$ is also embedded in α .

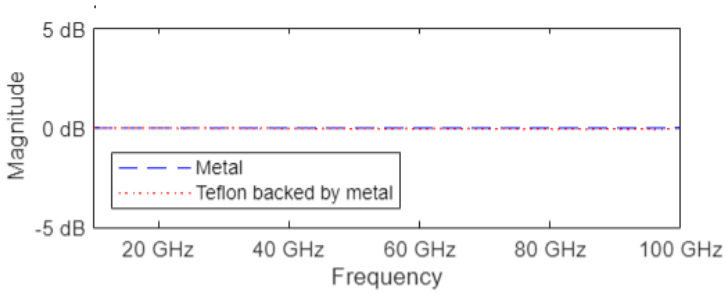

(a) Magnitude

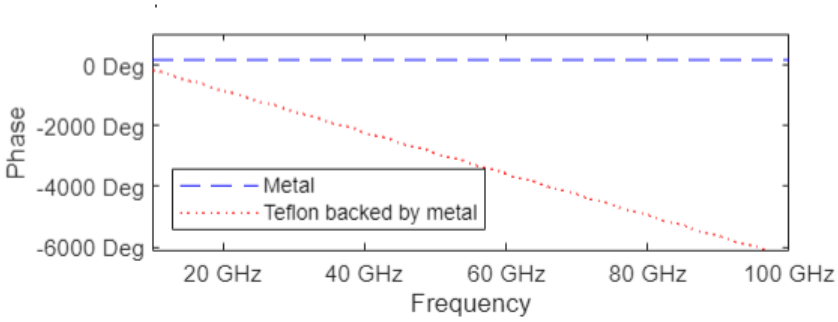

(b) Phase (Unwrapped)

Figure 3.15: A comparison between the magnitude and the unwrapped phase of Γ_{in} for a metal sample and a teflon sample backed by metal.

This simply means that the phase can be used alone for extracting those parameters or used with the magnitude information for enhancing the measurement accuracy. Another important detail that can be obtained from the phase in conjunction with the magnitude, is the layer configuration. For example, using both magnitude and phase information, a metal backed dielectric can be distinguished from metal only material as shown in Figure 3.15 for a 2cm thick Teflon sample. The phase information can also identify the lossy material backed by metal as shown in Figure 3.16 for 4cm thick lossy material with ε_r of 3 and tan δ of 0.1 .

For lossy materials, the attenuation is usually large enough so the magnitude decays significantly with frequency. This decay continues until the magnitude converges to a fixed value representing Γ_{12} which is the first reflection from the material. All other multiple reflection components are eventually attenuated inside the material. Similarly, the phase also starts to converge to a fixed value of $n\frac{\pi}{2}$ representing the phase of Γ_{12} as seen in Figure 3.16.

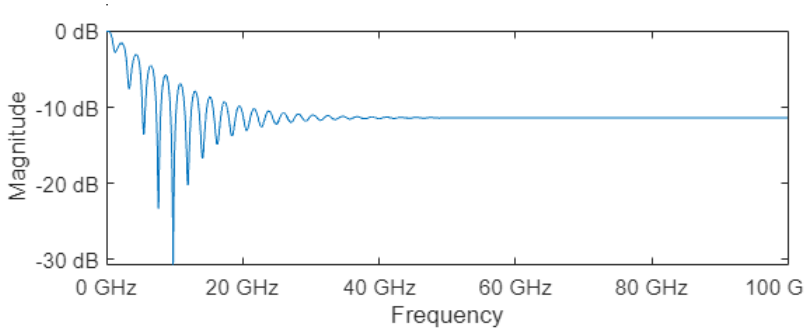

(a) Magnitude

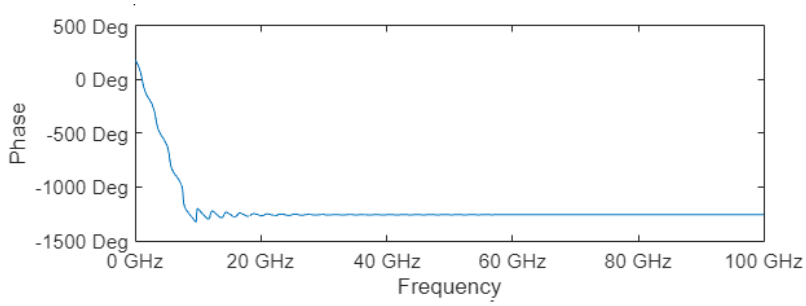

(b) Phase (Unwrapped)

Figure 3.16: Magnitude and unwrapped phase of Γ_{in} for a 4cm thick lossy material backed by metal.

Chapter 4

Radar Board

In this chapter, we are going to discuss the details of the radar board we are using for the material characterization measurements. FMCW radars are widely used today for many sensing applications such as automotive collision avoidance, tank level monitoring and consumer electronics. The high range resolution and the simple architecture and post processing makes FMCW radar a favourable option for these applications. The theory and principle of operation of FMCW radar was previously discussed in subsection 3.1.3. The FMCW radar board we are using is TI AWR2243BOOST radar evaluation board shown in Figure 4.1, which is based on AWR2243 radar chip. This board is mainly targeted towards automotive and short range radar imaging applications [22].

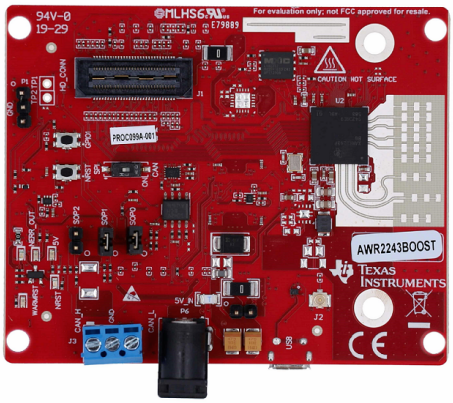

Figure 4.1: AWR2243BOOST FMCW radar board from Texas Instruments [42]

This radar board covers a 5 GHz sweeping bandwidth starting from 76 to 81 GHz with 3 Tx and 4 Rx channels. The radar also supports MIMO and phased-array modes for high resolution detection and imaging.

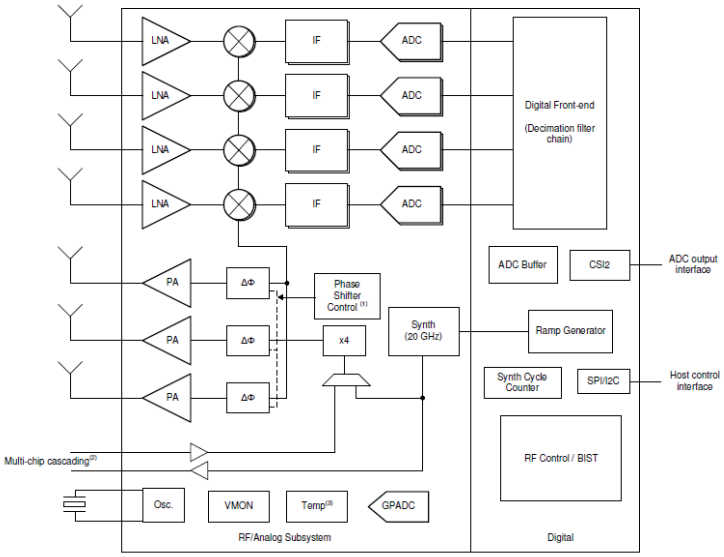

Figure 4.2: Functional block diagram for AWR2243 radar chip (© Texas Instruments) [42]

4.1 Complex Baseband Architecture

One of the interesting features of this radar board and the main reason for choosing it for our material characterization measurements is the complex baseband architecture. Normally, the demodulation of FMCW radar systems is performed using a real-only baseband architecture as shown in Figure 4.3.

In this architecture, the received signal is directly mixed with the instantaneous signal $\cos(\phi_T(t))$ of the local oscillator LO shown in Figure 4.4. The received signal represents attenuated and delayed versions of the LO signal for different targets. The desired information is located in the in-band part of the Rx signal spectrum, while the remaining spectrum (image band) contains only noise which is also spread across the in-band spectrum. After the mixing, the IF signal spectrum exhibits a noise foldback originated from the image-band noise. This noise foldback results in up to 3 dB degradation in the signal to noise ratio SNR of the IF signal.

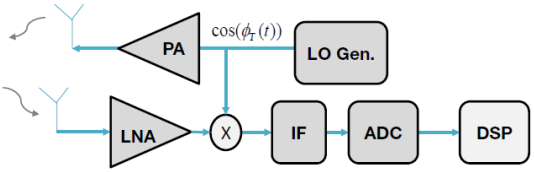

Figure 4.3: Block diagram for FMCW radar with real-only baseband architecture (© Texas Instruments) [42]

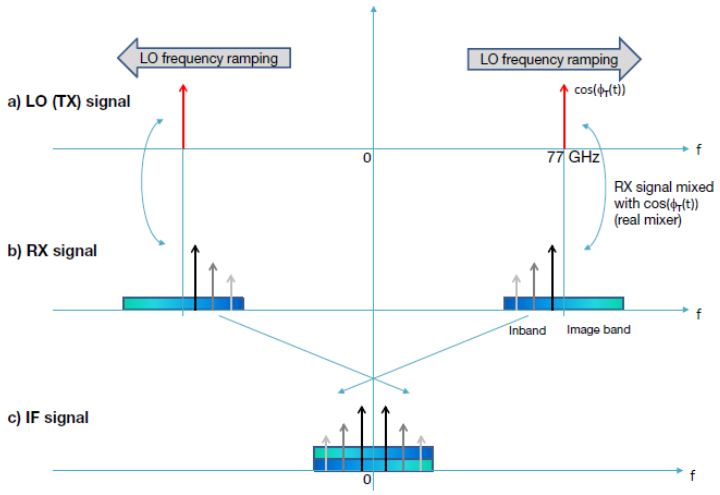

Figure 4.4: Spectrum of real mixer with baseband signal foldback. (a) Instantaneous LO signal spectrum (Tx), (b) Rx signal spectrum from multiple targets, (c) Baseband (IF) signal spectrum with foldback (© Texas Instruments) [42].

In complex baseband architecture, the received signal is divided between in-phase I and quadrature Q paths as shown in Figure 4.5. In the in-phase I path, the received signal is mixed with the same version of the instantaneous LO signal cos(phi(t)), while it is mixed with sin $(\phi_T(t))$in the quadrature Q path.

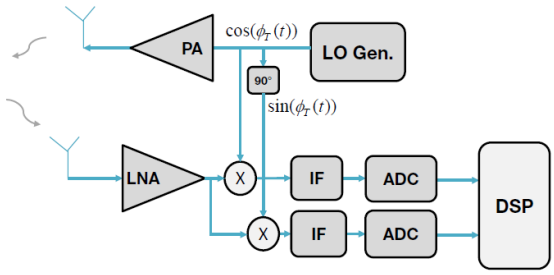

Figure 4.5: Block diagram for FMCW radar with complex baseband architecture (© Texas Instruments) [42].

Due to the quadrature mixing and the IQ baseband architecture, the resulting IF signal, seen in Figure 4.6, is not affected by the noise foldback seen with the real mixing which enhances the SNR of the IF signal by up to 3dB.

Other benefits for the complex baseband architecture include:

- Enhanced interference tolerance
- Lower intermodulation impact
- Enhanced functional safety monitoring

4.2 Chirp and Frame structure

The chirp signal transmitted from the FMCW radar represents a linear frequency sweep over a sweeping bandwidth B. Ideally, a train of these transmitted chirps would look similar to the chirps in Figure 3.12 with no separation period between the chirps and an instantaneous transition from f_{high} to f_{low}. However, in practice, and due to the hardware limitations,a separation time (Idle Time) between the subsequent chirps is needed for allowing enough transition from f_{high} to f_{low} as shown in Figure 4.7. The ADC also needs some time to start before sampling. The ADC sampling window represents the effective duration of the transmitted chirp at which the actual sweeping bandwidth is represented.

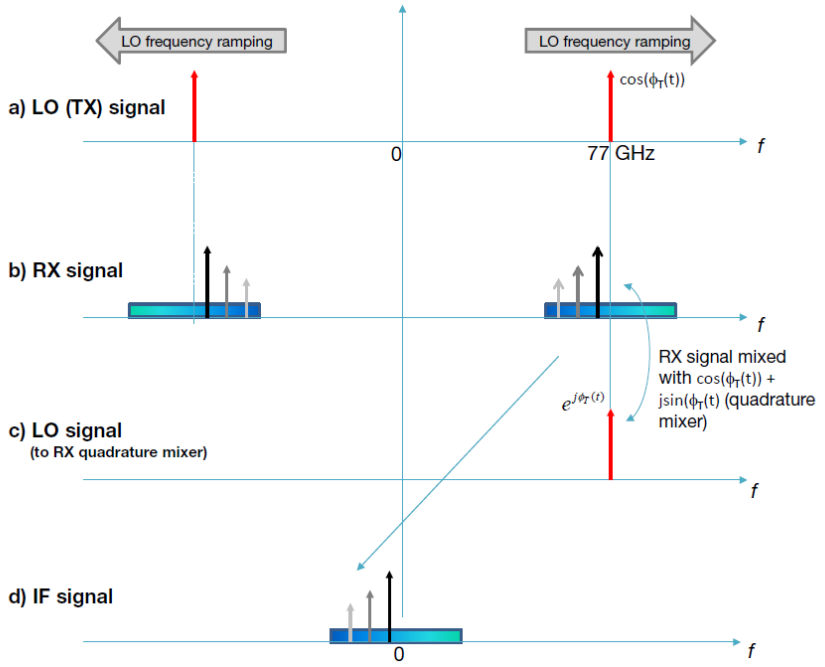

Figure 4.6: Spectrum of a quadrature mixer without baseband signal foldback. (a) Instantaneous LO signal spectrum (Tx), (b) Rx signal spectrum from multiple targets, (c) Complex LO signal spectrum, (d) Baseband (IF) signal spectrum without foldback (© Texas Instruments) [42].

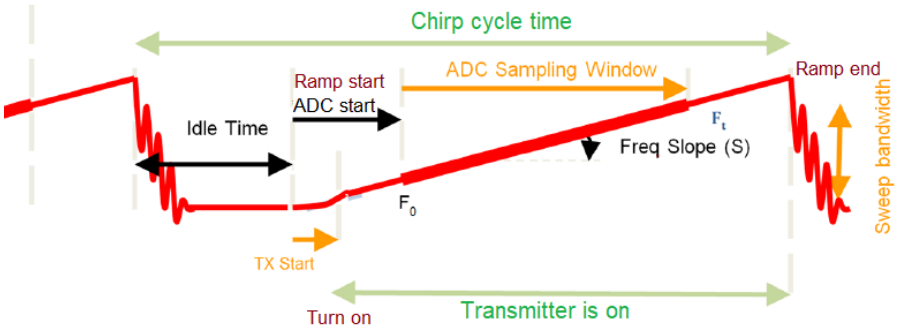

Figure 4.7: FMCW chirp structure (© Texas Instruments) [23].

The actual values chosen for our setup according to the manufacturer recommendation are presented in Table 4.1.

Tx start time	1 μs
Frequency slope	96.994 MHz/μs
Idle time	20 μs
ADC start time	5 μs
Effective bandwidth	4.41 GHz

Table 4.1: Actual chirp parameters and effective bandwidth used for our measurements

A set of subsequent chirps is called a "frame" which represents an observation window for post processing as seen in Figure 4.8. To allow the radar to collect enough reflections from the material after each chirp is sent, we choose a 1 chirp per frame configuration with a frame periodicity of 200 ms. For each measurement, 100 frames are sent towards the material and then averaged over the number of frames for minimizing the noise effects.

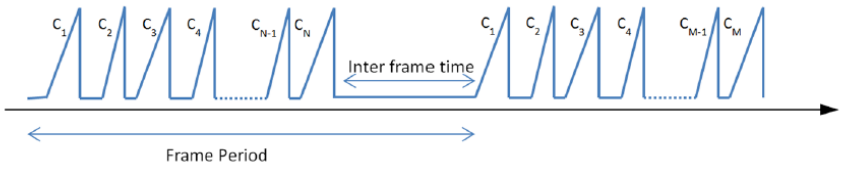

Figure 4.8: FMCW frame structure [23].

4.3 Antenna Front end

The radar board has 3 Tx and 4 Rx series-fed patch antenna arrays with two dummy antennas around the receiver as shown in Figure 4.9. The 3 Tx antennas are separated by λ while the 4 Tx antennas are separated by $\lambda/2$. Additionally, the middle Tx antenna is elevated by $\lambda/2$. This antenna configuration allows angular estimation for the target in azimuth and elevation in MIMO mode.

Each antenna has a gain of around 10 dB with an H-plane HPBW of 60° and E-plane HPBW of 26° degrees as shown in Figure 4.10. Due to the nature of the series-fed antenna arrays, the direction of the main lobe in elevation changes with frequency as shown in Figure 4.10. This change in the main lobe direction is not a significant problem

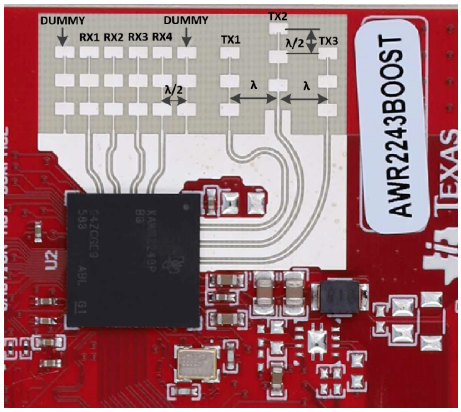

Figure 4.9: Antenna front end for AWR2243BOOST radar board.

for radar detection applications. However, for material characterization applications, the theoretical models assume a normal incidence on the surface of the material. Therefore, the change in the main lobe direction could generate errors especially with relatively long range measurements.

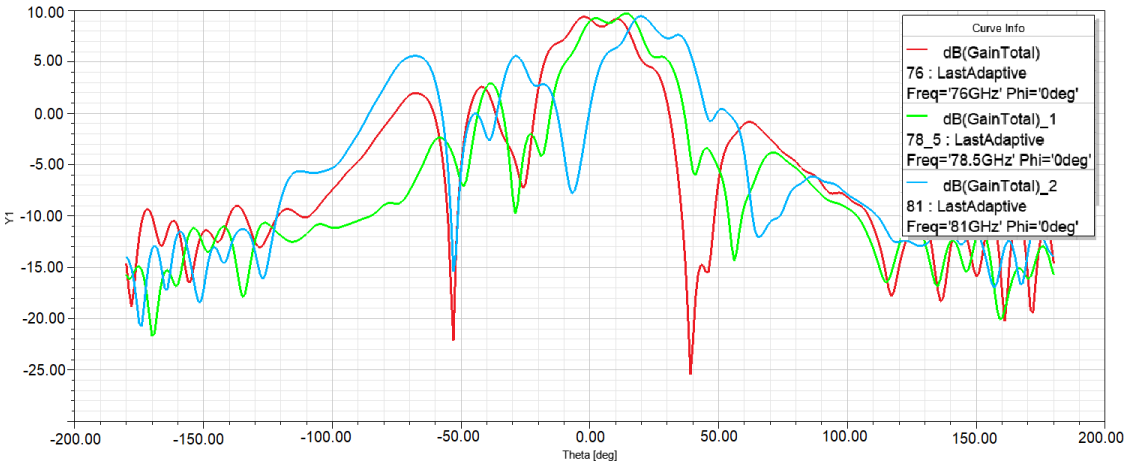

Figure 4.10: Simulation results of E-plane radiation pattern for single series-fed antenna array for 76, 78.5 and 81 GHz.

In order to overcome this problem, and for maximizing the reflections from the material under test, a dielectric lens is designed and fabricated for a better main beam collimation and enhancing the radar antenna gain. The details of the design and the fabrication of this lens are discussed in Chapter 5.

Chapter 5

Lens Design and Fabrication

In this chapter, we are presenting the dielectric lens antenna design and fabrication for enhancing the radar antenna gain and focusing the main beam over the whole band of interest. Dielectric lens antennas are commonly used in communications and radar applications for enhancing the antenna gain and boosting the range. There are various types of lenses (e.g., Hyperbolic, Elliptic, Fresnel, GRIN) depending on the principle of design. Various methods can be used for fabricating the lens structure, such as machining and 3D printing as discussed in [16] and [25]. While machining is better for design accuracy and surface finishing, 3D printing is a faster and cheaper option. The goal of our lens design is to achieve maximum gain while focusing the beam for a normal incidence on the material over the whole sweeping bandwidth of the radar. The focused beam of the hyperbolic lens is assumed to be plane wave as shown in Figure 5.2, which is a fundamental assumption in our theoretical models discussed in Chapter 3. Two design options were explored. The first design option is using a single large 3D-Printed Fresnel zone lens as seen in Figure 5.1, with a radius of 10cm, focal length 20cm and a focal point between Tx1 and Rx4 antennas. The lens dimensions along with the focal length are chosen so that a maximum gain is achieved within a specific setup dimensions of 20 cm, while achieving a minimum beam shift due to the location of the focal point between the two antennas. This design yields a gain of 30dB, however, due to the focal point location between the two antennas, the Tx and Rx beams are tilted horizontally by a small angle which generates errors with long ranges. Additionally, the far field zone for this design starts beyond 20m due to the large size of the lens, according the far-field region equations in [38].

The second design option is using two identical hyperbolic 3D-Printed lenses for the two antennas. The lens design started with a trade off between the lens size, the focal length and the gain. In order to allow enough space for each lens and minimizing the overlap,

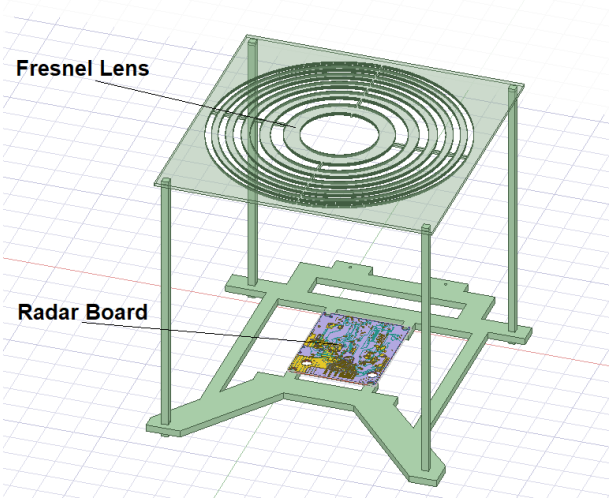

Figure 5.1: First design option using a large Fresnel zone lens

the two antennas used were the furthest Tx and Rx antennas (Tx3 and Rx1). The design of the hyperbolic profile of the lens, shown in Figure 5.2, is based on equation 5.1 which relates the profile of the lens $\rho(\psi)$ to the refractive index n , and the focal length f with angle ψ.

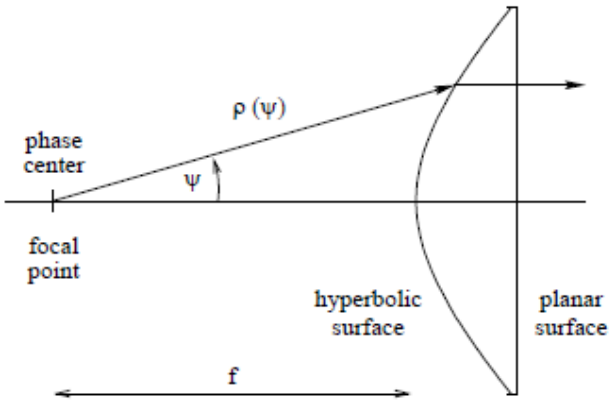

Figure 5.2: Hyperbolic lens geometry [36].

$$\rho(\psi) = \frac{(n-1)f}{n\cos\psi - 1} \tag{5.1}$$

In order to minimize the reflections from the antenna structure, a 3D-printing PLA material with a dielectric constant of 3 is chosen. The choice of this specific material is made in order to minimize the reflections coming back from the lens structure due to the contrast between the permittivity of the lens and free-sapce. The profile of the lens $\rho(\psi)$ can then be calculated using equation 5.1.

The radius of each single lens is optimized for minimum overlap between the two lenses and maintaining a relatively high gain. The radius is chosen to be 12mm with a focal length of 7mm. The initial design for a single lens is generated in 3D on HFSS simulation software as seen in Figure 5.3.

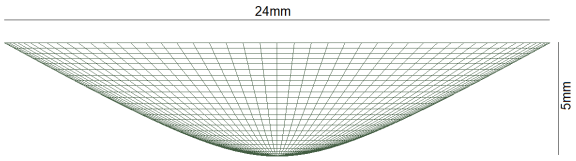

Figure 5.3: Initial hyperbolic lens design

The design is further optimized in elevation in order to cover the main beam of the antenna underneath for the whole sweeping bandwidth. This optimization is performed by extending the lens body in elevation by various lengths in order to find the extension length that matches the antenna beam to the lens for all frequencies. The optimum extension is found to be 2.5mm in elevation as shown in Figure 5.4(a). The two lens structures for Tx and Rx antennas are then accurately positioned and attached together as seen in 5.4(b). The model is then simulated using HFSS for extracting the gain and confirming the main beam angle correction.

The simulation results are presented in Figure 5.5. The maximum gain is equal to 18 dB with the main beam direction corrected for the entire sweeping bandwidth compared to results in Figure 4.10.

In order to fix this dual lens structure with the radar board and maintain an accurate alignment with the on-board antennas, a holder structure is designed and fabricated. The holder fixes the dual antenna structure to a frame through four beams. Moreover, The frame is mounted on two sliding pillars which are attached to a holder mounted to the radar board through screws as seen in Figure 5.6.

The lenses along with the holder structure are finally fabricated using the high resolution Raise3D Pro2 3D printer. The fabricated dual lenses structure attached to the holder are shown in Figure 5.7. The complete printed structure attached to the radar board can also seen in Figure 5.8.

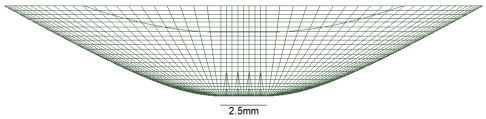

(a) Side view for a single lens

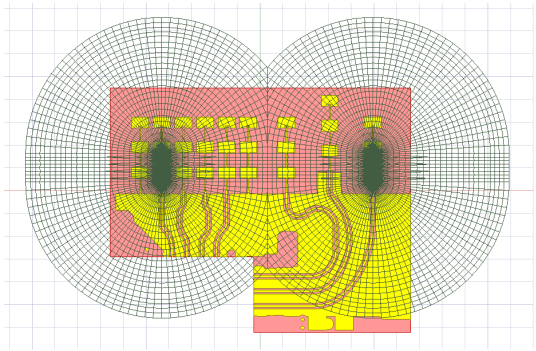

(b) Top view

Figure 5.4: Final optimized hyperbolic lens design, (a) Side view for a single lens with 2.5mm extension, (b) Top view for the dual lenses aligned to the on-board antennas underneath.

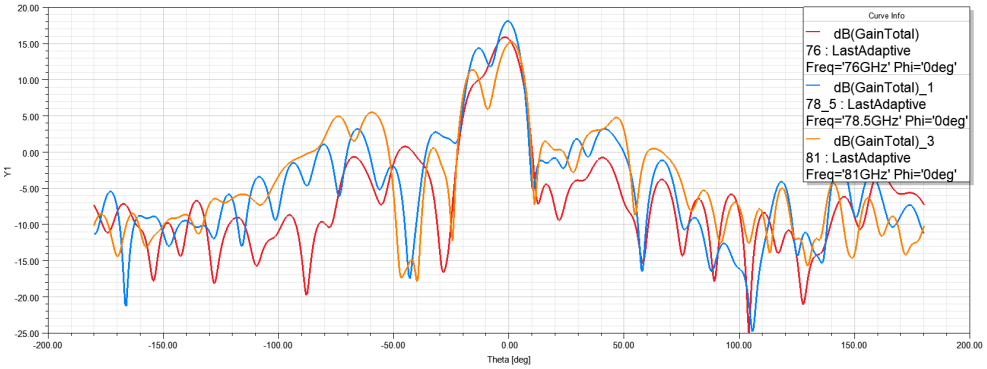

Figure 5.5: Simulation results of E-plane radiation pattern for single series-fed antenna radar with the hyperbolic lens structure for 76, 78.5 and 81 GHz.

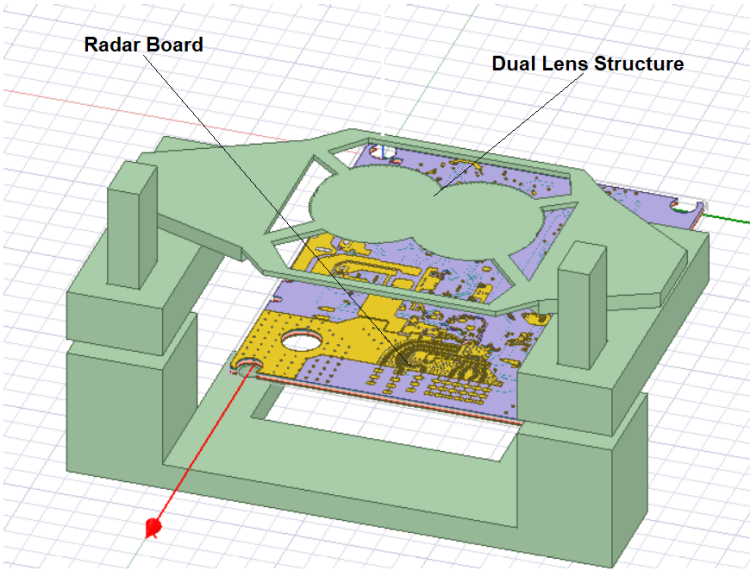

Figure 5.6: The dual lenses structure supported by the holder and attached to the radar board.

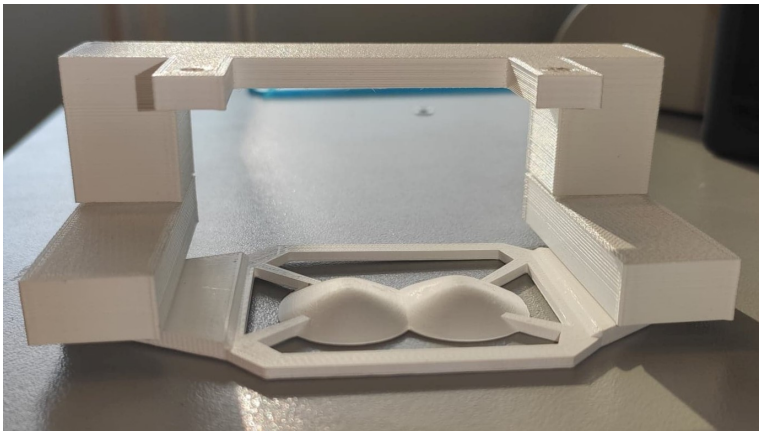

Figure 5.7: 3D-printed lens structure with the holder.

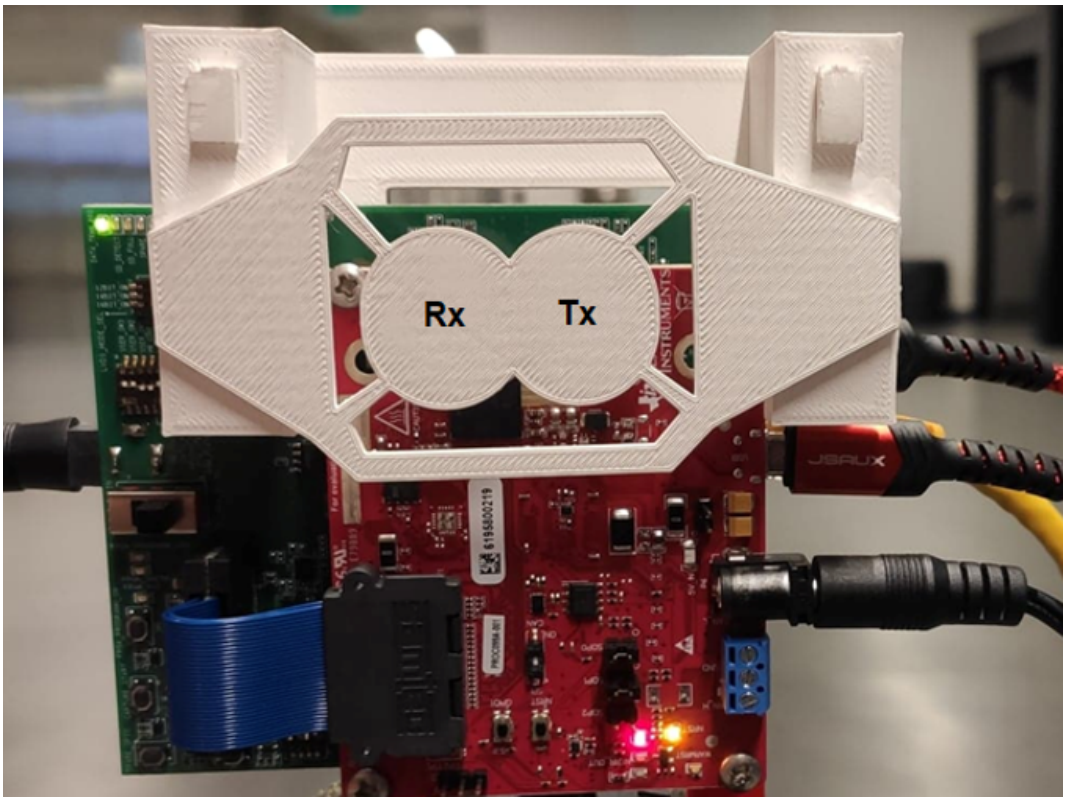

Figure 5.8: The dual lenses structure attached to the radar board through the holder.

Chapter 6

Experimental Results

In this chapter, we are discussing the test setup and presenting the calibration steps and the experimental test results. An additional discussion regarding the test challenges is also presented.

6.1 Setup Overview

Our experimental test setup is an actual representation for the setup model seen in Figure 3.2. The setup consists of the radar board with the lens attached to it and connected to a laptop for post processing. The radar board is mounted on an adjustable tripod for stabilization and accurate alignment to the material sample. The material sample is mounted on a wooden holder that provides stabilization and allows easy replacement and adjustment for the sample. The complete measurement setup is shown in Figure 6.1.

6.2 Calibration

The calibration step is essential for removing the effects of the channel and any distortion for the magnitude and phase that may affect the measured Γ_{in} results. The theory and a more detailed discussion about the calibration procedure was introduced in Section 3.2. For this section, we are presenting the actual implementation of the calibration process discussed before. The first step for the calibration is measuring the reflection coefficient $\Gamma_{m-match}$ while the material is removed as seen in Equation 3.42. This calibration step is needed for

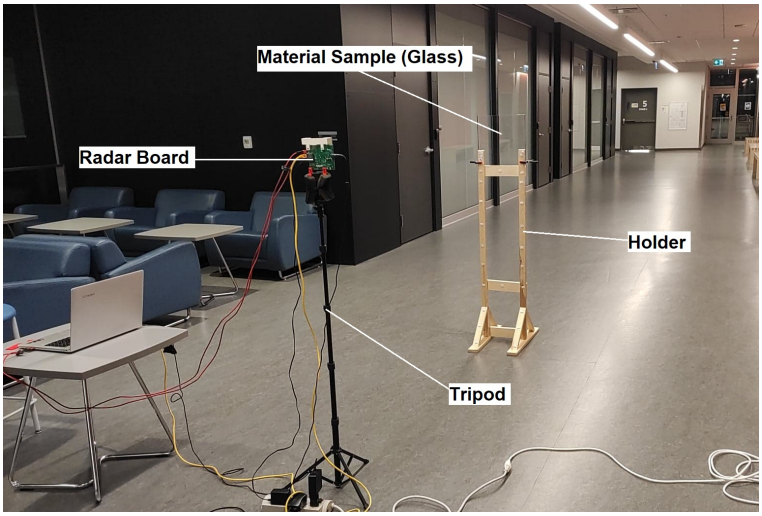

Figure 6.1: Experimental material characterization setup .

removing the effect of the material holder and the reflections from the environment. The second step in the calibration process is measuring the reflection coefficient $\Gamma_{m-short}$ by replacing the material sample with its metallic equivalent. This metallic equivalent, seen in Figure 6.2(a), is simply an aluminum plate with the same dimensions of the material sample (12"x12"). The final calibration step is shifting the metallic plate used in the previous step by a known distance Δd to extract Γ_{m-line} according to Equation 3.43. This shift is created by placing two 3D-Printed plastic pieces with a known thickness of 3mm between the metallic plate and the holder as shown in Figure 6.2(b). It is worth mentioning that any error in estimating the shift distance Δd would correspond to a linear phase distortion of $2\omega\frac{\Delta l}{c}$, where Δl is the error in the estimated shift. After the calibration steps, the measurement reference plane is translated to the surface of the material sample. The complex reflection coefficient of the material Γ_{in} can then be accurately measured.

In order to validate the quality of the calibration process, the metallic plate is placed again and its reflection coefficient is measured. Another measurement is taken while there is no material on the holder. Ideally, we should expect a flat line at 0 dB for the reflection coefficient magnitude of the metal and -∞ for the magnitude of the reflection coefficient while no material on holder .The results of those two tests, presented in Figure 6.3, confirm the accuracy of the calibration with the magnitude of Γ_{in} for the metal is almost 0 dB and the magnitude of Γ_{in} with no material, is around -40 dB.

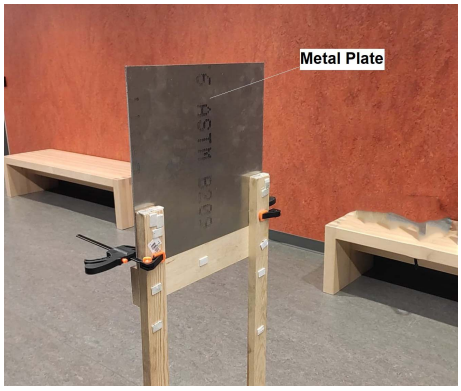

(a) Metal plate used for $\Gamma_{m-short}$ measurement.

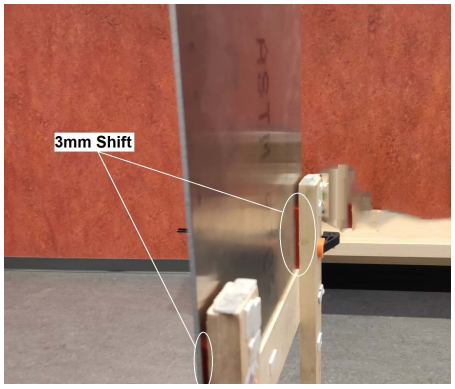

(b) Plastic pieces used for Γ_{m-line} measurement.

Figure 6.2: Calibration procedure (a) Extracting $\Gamma_{m-short}$ using metallic plate with the same dimensions of the material sample, (b) Extracting Γ_{m-line} by shifting the metallic plate using a 3mm thick plastic piece.

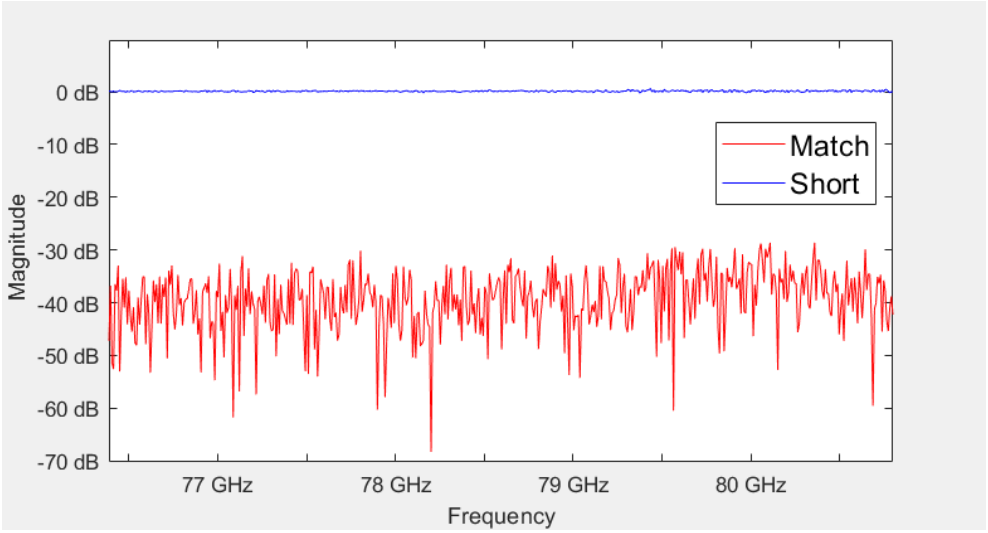

Figure 6.3: Magnitude of Γ_{in} for match and short measurments.

6.3 Measurement Results

In this section, we are introducing the test results for two dielectric materials with different dielectric properties and thicknesses. The first material is High-density polyethylene (HDPE) plastic which is widely used for manufacturing bottles and pipes. The second material is Poly(methyl methacrylate) (PMMA) which is also known as "Acrylic". The purpose of the two tests is to extract the dielectric properties (ε_r, tanδ), and thickness of each sample using the two extraction methods discussed in Section 3.3, and to compare the extracted parameters with the actual parameters reported in literature for verifying the effectiveness of our technique.

6.3.1 HDPE

The first sample used for testing is a flat plate of HDPE plastic material with (12"x12") dimensions and 1" thickness shown in Figure 6.5. This material has a dielectric constant ε_r of 2.3 and a loss tangent tanδ of 0.0003. The material is placed at a distance of 2m away from the radar. This distance is found to be the optimum distance for our setup for accurate measurements. Measuring the reflection coefficient Γ_{in} for a material sample that is closer than 2m was found to be generating magnitude and phase distortion due to the significant multiple reflection components between the radar board and the material surface, generating high frequency components in the FMCW radar baseband as shown in Figure 6.4. On the other hand, measuring Γ_{in} for a material placed further than 2 meters was found to be also generating errors in the magnitude and phase as the beam width becomes large enough to collect unwanted reflections from the environment around the setup, and also due to the low SNR of the received signal.

The complex reflection coefficient Γ_{in} results from the test at 2m are presented in Figure 6.6. The frequency band starts at 76.38 GHz to 80.8GHz which represents the effective bandwidth of the radar board with the chosen chirp parameters as discussed in Section 4.2.

Using the maxima and minima method introduced in Section 3.3, the extracted dielectric constant is found to be equal to 2.44. The order of the first maxima is calculated from the frequency difference between the maximum and minimum of $|\Gamma_{in}|$ and is found to be equal to 21. The thickness is then extracted using Equation 3.52 and is calculated to be equal to 2.63 cm. Using the non-linear least squares curve fitting method, the magnitude of Γ_{in} is first fitted using multiple initial values for ε_r, tanδ and the thickness d, until finding the values achieving the best fit. Those values can then be used as initial values for

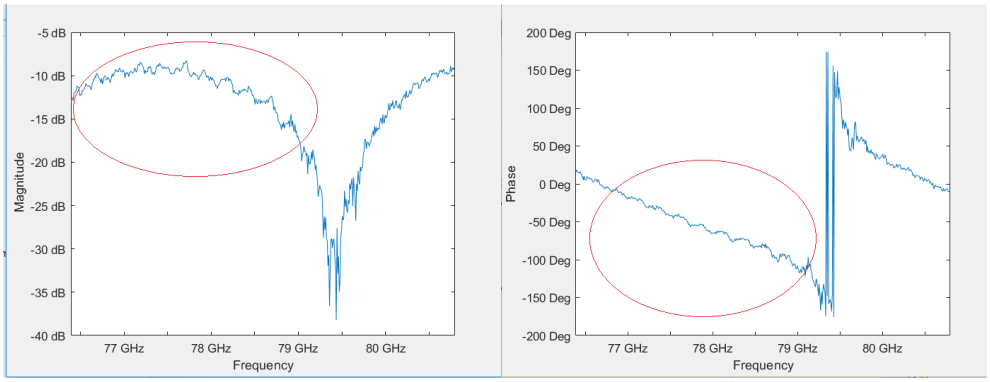

Figure 6.4: The magnitude and phase distortions resulting from the multipe reflections between the radar and the sample for a 1 m distance.

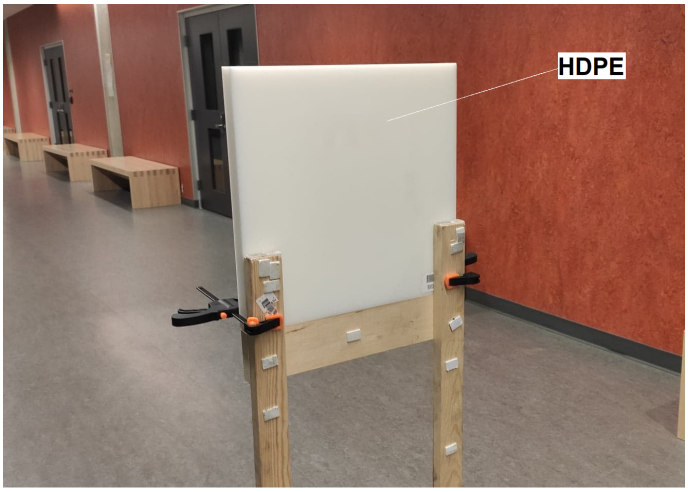

Figure 6.5: HDPE sample.

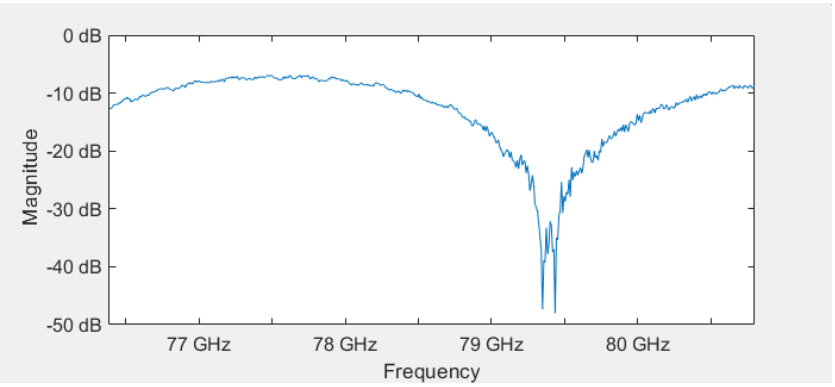

(a) Magnitude

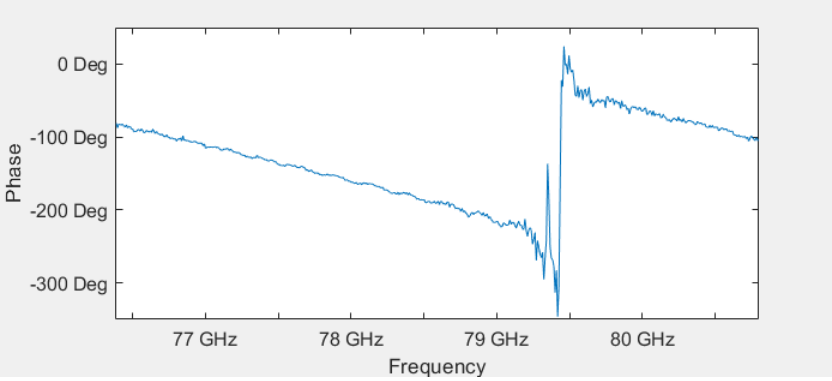

(b) Phase (Unwrapped)

Figure 6.6: Measured magnitude and unwrapped phase of Γ_{in} for a 12"x12"x1" HDPE sample.

the curve fitting on the phase of Γ_{in}. The values of ε_r, and d extracted from the Maxima and Minima method can also be used as initial values for the curve fitting on either the magnitude or phase of Γ_{in}. The fitting of both the magnitude and phase of Γ_{in} is presented in Figure 6.7.

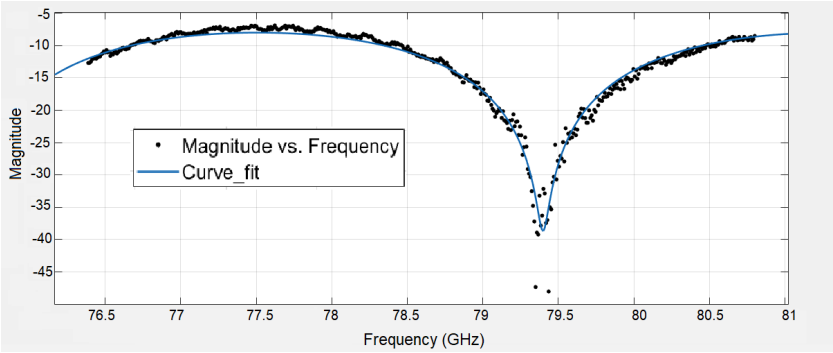

(a) Magnitude

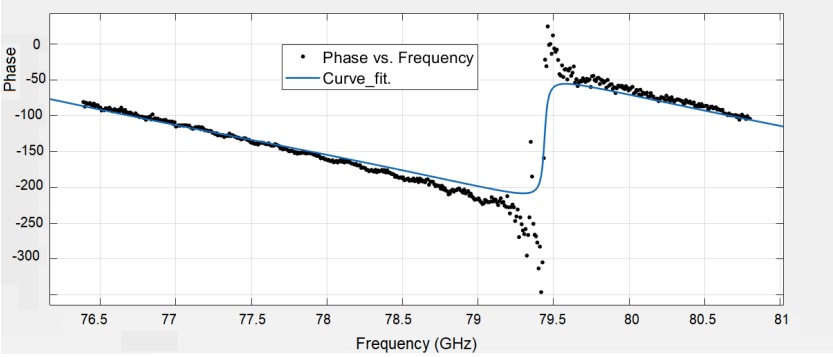

(b) Phase (Unwrapped)

Figure 6.7: Curve fitting on the magnitude and phase of Γ_{in} for the HDPE sample.

The extracted dielectric properties and thickness of the HDPE sample with the curve fitting method using the magnitude and the phase are presented in Table 6.1 along with the values extracted from the maxima and minima method and the actual dielectric properties of HDPE from the literature. The results show that while the maxima and minima method is simple and fast, the curve fitting method is more accurate. Moreover, the maxima and minima method can be more useful for extracting the initial values for the curve fitting method for quickly reaching an accurate fit. Both methods, however, confirm the effectiveness of the FMCW complex baseband methods.

Parameter	Maxima and Minima	Curve fit (Magnitude)	Curve fit (Phase)	Actual
ε_r	2.44 (6%)	2.378 (3.3%)	2.27 (1.3%)	2.3
tanδ	N/A	0.0008 (166%)	0.0004 (33%)	0.0003
d (cm)	2.63 (3.5%)	2.57 (1.1%)	2.50 (1.5%)	2.54 (1")

Table 6.1: Measurement results for the dielectric parameters of the HDPE sample using the maxima and minima method and the curve fitting method, and compared with the actual values from literature. The error percentage in each measurement is indicated between parentheses.

6.3.2 PMMA

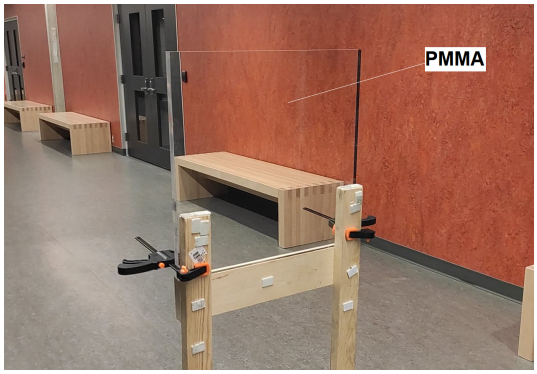

Figure 6.8: PMMA sample.

The second sample used is a flat PMMA plate with similar dimensions to the HDPE sample (12"x12") and half the thickness (0.5"). This material has a dielectric constant ε_r of 2.6 and loss tangent tanδ of 0.012. The material is placed at the same holder with the same distance away from the radar, similar to the HDPE sample. The measured magnitude and phase of Γ_{in} along with the curve fitting are presented in Figure 6.9. Using the maxima and minima method, the dielectric constant is calculated to be equal to 2.08 .The thickness is also found to be equal to 1.49 cm. Those values are then used as initial values for the curve fitting method. The extracted parameters using the two methods are presented in Table 6.2.

It can be noted that the accuracy of the maxima and minima method is relatively lower for this test. The reason for this low accuracy is that the minima and maxima method assumes that the material under test is lossless. However, PMMA has relatively high losses

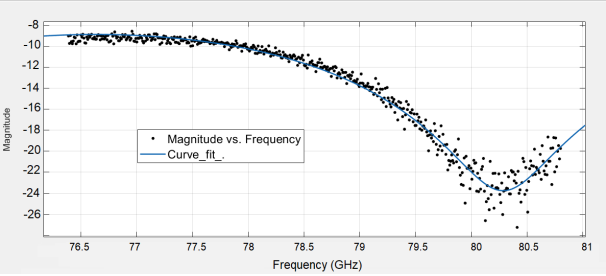

(a) Magnitude

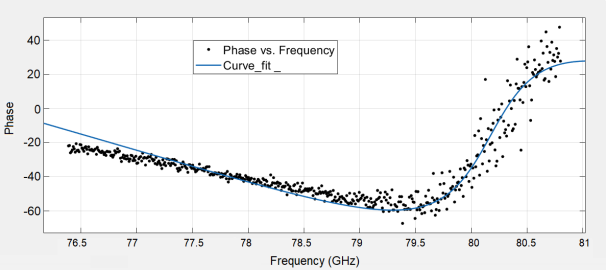

(b) Phase (Unwrapped)

Figure 6.9: Curve fitting on the magnitude and phase of Γ_{in} for the PMMA sample.

(tanδ =0.012). In contrast, the accurate results obtained using the curve fitting method proves the effectiveness of this technique for lossless and lossy materials.

Parameter	Maxima and Minima	Curve fit (Magnitude)	Curve fit (Phase)	Actual
ε_r	2.08 (20%)	2.4 (7.6%)	2.5 (3.8%)	2.6
tanδ	N/A	0.0099 (17.5%)	0.0099 (17.5%)	0.012
d (cm)	1.49 (14.6%)	1.32 (1.5%)	1.3 (0%)	1.3 (0.5")

Table 6.2: Measurement results for the dielectric parameters of the PMMA sample using the maxima and minima method and the curve fitting method, and compared with the actual values from literature. The error percentage in each measurement is indicated between parentheses.

Chapter 7

Conclusions and Future Work

In this thesis, we demonstrated the ability of remotely characterizing materials with high accuracy using a complex baseband FMCW radar. We started with an introduction and literature review of the current techniques and methods used for material characterization with the advantages and drawbacks of each technique. We presented a detailed analysis of the system with three different models that mathematically explain the behaviour of the system and predict the challenges for obtaining accurate measurement results. These models were verified using MATLAB simulation with a complete consistency across all the models. Moreover, a discussion regarding the importance of using the phase information for enhancing the measurement accuracy and providing extra information about the material was introduced. Two different methods for extracting the dielectric properties of the material from the measurements were explained. Finally, we tested our models and complete system in practice with two different material samples placed at 2m away from the radar system. The extracted results proved the accuracy of the system for remotely measuring the dielectric parameters and thickness of materials with high accuracy using a compact and cheap FMCW radar system. Our setup has an accuracy comparable with expensive VNA based material characterization systems used in research labs. Our early study paves the way for unlimited innovations and applications in many fields, such as automotive, smart homes, food quality and production lines.

7.1 Future Work

One of the limitations of our system is the on-board antenna front end design. In order to characterize materials at ranges beyond 2m, a completely redesigned antenna front end and

a new larger lens with higher gain are needed. The calibration process before starting the measurement consumes time and is sensitive to errors. An automatic calibration method that estimates the channel error effects and the RCS of the sample in real time would be an optimal solution for making the system more practical and commercially viable. Such a system would rely on an extra sensor that can estimate the RCS of the material under test, and use the radar range measurements along with the predetermined antenna gains in order to model and automatically calibrate the system. Another interesting feature of the radar board used is the MIMO beamforming. Utilizing this feature may enhance the measurement accuracy and allow measurement at longer ranges with smaller sample dimensions. Finally, a comprehensive study for the theoretical and practical system limitations (e.g., minimum thickness that can be measured), is needed for a complete assessment for the system.

References

[1] Abanob Abdelnour, Ahmed Rennane, Darine Kaddour, and Smail Tedjinio. Non-destructive dielectric characterization method for food products. *IEEE MTT-S International Microwave Symposium (IMS)*, 2017.

[2] Zaki Abdurrasyid and Achmad Munir. Characterization of thin slab artificial dielectric material using rectangular waveguide. *International Conference on Computer, Control, Informatics and Its Applications (IC3INA)*, 2014.

[3] Nabila Aouabdia, Nour Eddine Belhadj-Tahar, and Georges Alquié. Rectangular patch resonator sensors for characterization of biological materials. *IEEE 11th International Multi-Conference on Systems, Signals and Devices (SSD14)*, 2014.

[4] James Baker-Jarvis, Michael D. Janezic, Bill Riddle, Christopher L. Holloway, N.G. Paulter, and J.E. Blendell. *Dielectric and Conductor-Loss Characterization and Measurements on Electronic Packaging Materials.* National Institute of Standards and Technology, 2001.

[5] Constantine A. Balanis. *Advanced Engineering Electromagnetics, 2nd Edition.* Wiley, 2012.

[6] Jan Barowski and Ilona Rolfes. Millimeter wave material characterization using FMCW-transceivers. *IEEE MTT-S International Microwave Workshop Series on Advanced Materials and Processes (IMWS-AMP 2017)*, 2017.

[7] Jan Barowski, Marc Zimmermanns, and Ilona Rolfes. Millimeter-wave characterization of dielectric materials using calibrated FMCW transceivers. *IEEE Transactions on Microwave Theory and Techniques*, 66(8), 2018.

[8] W. Burnside and K. Burgener. High frequency scattering by a thin lossless dielectric slab. *IEEE Transactions on Antennas and Propagation*, 31(1), 1983.

[9] Kevin Khee-Meng Chan, Adrian Eng-Choon Tan, Lin Li, and Karumudi Rambabu. Material characterization of arbitrarily shaped dielectrics based on reflected pulse characteristics. *IEEE Transactions on Microwave Theory and Techniques*, 63(5):891–921, 2015.

[10] Akin Dalkilic, Doganay Dogan, and M. Erim Inal. Characterization and design of elastomeric magnetodielectric materials for radar absorber structures. *Symposium of the International Union of Radio Science (URSI GASS)*, 2017.

[11] R. A. Fenner, E. J. Rothwell, and L. L. Frasch. A comprehensive analysis of free-space and guided-wave techniques for extracting the permeability and permittivity of materials using reflection-only measurements. *Radio Science*, 47, 2012.

[12] R. A. Fenner, E. J. Rothwell, and L. L. Frasch. A comprehensive analysis of free-space and guided-wave techniques for extracting the permeability and permittivity of materials using reflection-only measurements. *Radio Science*, 47, 2012.

[13] N.H. Osman; C.E. Free. Method for characterizing dual-layer materials using a free space technique. *Asia-Pacific Microwave Conference*, 2010.

[14] B.W. Hakki and P.D. Coleman. A dielectric resonator method of measuring inductive capacities in the millimeter range. *IRE Transactions on Microwave Theory and Techniques*, 8(4), 1960.

[15] M.J. Havrilla and D.P. Nyquist. Electromagnetic characterization of layered materials via direct and de-embed methods. *IEEE Transactions on Instrumentation and Measurement*, 55(1), 2006.

[16] A. M. Hegazy, M. A. Basha, and S. Safavi-Naeini. 3D-printed scanning dielectric lens antenna. *2019 IEEE International Symposium on Antennas and Propagation and USNC-URSI Radio Science Meeting*, 2019.

[17] Ahmed M. Hegazy, Mustafa M. Mosaad, and Ayman M. Hassan. FMCW software defined radar for range and speed estimation. *First International Undergraduate Research Conference, IUGRC, 2016*, 1, 2016.

[18] Hristo D. Hristov. *Fresnel Zone Plate Antenna*. Springer Science, 2016.

[19] Milo W. Hyde and Michael J. Havrilla. Broadband, nondestructive characterization of PEC-backed materials using a dual-ridged-waveguide probe. *USNC-URSI Radio Science Meeting (Joint with AP-S Symposium)*, 2013.

[20] Texas Instruments. MIMO radar, SWRA554A application report. 2017.

[21] Texas Instruments. Using a complex-baseband architecture in FMCW radar systems. 2017.

[22] Texas Instruments. AWR1243 sensor: Highly integrated 76–81-GHz radar front-end for emerging ADAS applications. 2019.

[23] Texas Instruments. Programming chirp parameters in TI radar devices,, Application note. 2020.

[24] Texas Instruments. AWR2243 single-chip 76- to 81-GHz FMCW transceiver datasheet (Rev. A). 2020.

[25] Kyoung Ho Jeong and Nima Ghalichechian. 3D-printed 4-zone Ka-band fresnel lens: design, fabrication, and measurement. *IET Microwaves, Antennas and Propagation*, 2019.

[26] Abhishek Kumar Jha and M. Jaleel Akhtar. SIW cavity based RF sensor for dielectric characterization of liquids. *2014 IEEE Conference on Antenna Measurements & Applications (CAMA)*, 2014.

[27] Michel Joussemet. Novel devices and material characterization at mm-Wave and terahertz. *Agilent Technologies*.

[28] Cynthia Junqueira, Marcelo Perotoni, and Daniela Ronsó Lima. Microwave absorber materials characterization: bulk absorbing and electrical/magnetic parameters. *2014 International Telecommunications Symposium (ITS)*, 2014.

[29] Cynthia Junqueira, Marcelo Perotoni, and Daniela Ronsó Lima. Microwave absorber materials characterization: bulk absorbing and electrical/magnetic parameters. *International Telecommunications Symposium (ITS)*, 2014.

[30] Alireza Kazemipour, Martin Hudlička, Mohammed Salhi, Thomas Kleine-Ostmann, and Thorsten Schrader. Free-space quasi-optical spectrometer for material characterization in the 50–500 ghz frequency range. *44th European Microwave Conference*, 2014.

[31] Alireza Kazemipour, See-Khee Yee, Martin Hudlička, Mohammed Salhi, Thomas Kleine-Ostmann, and Thorsten Schrader. Design and calibration of a compact quasi-optical system for material characterization in millimeter/sub-millimeter wave do-

main. *29th Conference on Precision Electromagnetic Measurements (CPEM 2014)*, 2014.

[32] E. Kemptner and S. Thurner. Free space material characterization for microwave frequencies. *6th European Conference on Antennas and Propagation (EUCAP)*, 2012.

[33] Jri Lee, Yi-An Li, Meng-Hsiung Hung, and Shih-Jou Huang. A fully-integrated 77-GHz FMCW radar transceiver in 65-nm CMOS technology. *IEEE Journal of Solid-State Circuits*, 45(12), 2010.

[34] Humberto Lobato-Morales, Alonso Corona-Chávez, José Luis Olvera-Cervantes, Ricardo Arturo Chávez-Pérez, and José Luis Medina-Monroy. Wireless sensing of complex dielectric permittivity of liquids based on the RFID. *IEEE Transactions on Microwave Theory and Techniques*, 62(9), 2014.

[35] Takuya Nozawa, Yuya Makino, Nobuyuki Takaya, Masahiro Umehira, Shigeki Takeda, Xiaoyan Wang, and Hiroshi Kuroda. An anti-collision automotive fmcw radar using time-domain interference detection and suppression. *International Conference on Radar Systems (Radar 2017)*, 2017.

[36] Petr Piksa, Stanislav Zvanovec, and Petr Cenry. Elliptic and hyperbolic dielectric lens antennas in mm-waves. *Radio Engineering*, 20(1), 2011.

[37] L. Pometcu, A. Sharaiha, R. Benzerga, R. D. Tamas, and P. Pouliguen. Method for material characterization in a non-anechoic environment. *Applied Physics Letters*, 108(16), 2016.

[38] David M. Pozar. *Microwave Engineering, 4th Edition*. Wiley, 2011.

[39] Karthik Ramasubramanian and Brian Ginsburg. AWR1243 sensor: Highly integrated 76–81-GHz radar front-end for emerging ADAS applications. *Texas Instruments*, 2017.

[40] A.G. Stove. Linear FMCW radar techniques. *IEE Proceedings F - Radar and Signal Processing*, 139(5), 1992.

[41] Keysight Technologies. De-embedding and embedding S-Parameter networks using a vector network analyzer, Application note. 2017.

[42] S. Thomas, C. Bredendiek, T. Jaeschke, F. Vogelsang, and N. Pohl. A compact, energy-efficient 240 GHz FMCW radar sensor with high modulation bandwidth. *2016 German Microwave Conference (GeMiC)*, 2016.

[43] Jonas Wagner, Jan Barowski, and Ilona Rolfes. A 3d printed elliptical mirror for material characterization using fmcw transceivers. *Asia-Pacific Microwave Conference (APMC)*, 2018.

[44] Danang Primaadi Wibowo and Achmad Munir. 3D artificial material characterization using rectangular waveguide. *International Conference on Information Technology and Electrical Engineering (ICITEE)*, 2014.

[45] JKuek Chee Yaw. *Measurement of Dielectric Material Properties, Application Note*. Rohde & Schwarz, 2012.

[46] Kok Yeow You. *Microwave Systems and Applications*, chapter Materials Characterization Using Microwave Waveguide System. IntechOpen, 2016.

[47] Dmitry Zelenchuk and Vincent Fusco. Dielectric characterisation of pcb materials using substrate integrated waveguide resonators. *The 40th European Microwave Conference*, 2010.

[48] S. Zinal and G. Boeck. Complex permittivity measurements using te/sub 11p/ modes in circular cylindrical cavities. *IEEE Transactions on Microwave Theory and Techniques*, 53(6), 2005.